Inelastic electron tunneling process for alkanethiol self-assembled monolayers

Inelastic electron tunneling process for alkanethiol self-assembled monolayers

Norio Okabayashi[1,*], Magnus Paulsson[2,†] and Tadahiro Komeda[3,‡]

[1]School of Mathematics and Physics, Kanazawa University, Kanazawa, Ishikawa 920-1192, Japan
[2]School of Computer Science, Physics and Mathematics, Linnaeus University, 391 82 Kalmar, Sweden
[3]Institute of Multidisciplinary Research for Advanced Materials (IMRAM), Tohoku University, Sendai, Miyagi 980-8577, Japan

[*]E-mail: okabayashi@staff.kanazawa-u.ac.jp
[†]E-mail: magnus.paulsson@lnu.se
[‡]E-mail: komeda@tagen.tohoku.ac.jp

Abstract

Recent investigations of inelastic electron tunneling spectroscopy (IETS) for alkanethiol self-assembled monolayers (SAMs) are reviewed. Alkanethiol SAMs are usually prepared by immersing a gold substrate into a solution of alkanethiol molecules, and they are very stable, even under ambient conditions. Thus, alkanethiol SAMs have been used as typical molecules for research into molecular electronics. Infrared spectroscopy and electron energy loss spectroscopy (EELS) have frequently been employed to characterize SAMs on the macroscopic scale. For characterization of alkanethiol SAMs on the nanometer scale region, or for single alkanethiol molecules through which electrons actually tunnel, IETS has proven to be an effective method. However, IETS experiments for alkanethiol SAMs employing different methods have shown large differences, i.e., there is a lack of standard data for alkanethiol SAMs with which to understand the IET process or to satisfactorily compare with theoretical investigations.

An effective means of acquiring standard data is the formation of a tunneling junction with scanning tunneling microscopy (STM). After explanation of the STM experimental techniques, standard IETS data are presented whereby a contact condition between the tip and SAM is tuned. We have found that many vibrational modes are detected by STM-IETS, as is also the case for EELS. These results are compared with IET spectra measured with different tunneling junctions. In order to precisely investigate which vibrational modes are active in IETS, isotope labeling of alkanethiols with specifically synthesized isotopically substituted molecule has been examined. This method provides unambiguous assignments of IET spectra peaks and site selectivity for alkanethiol SAMs such that all parts of the alkanethiol molecules almost equally contribute to the IET process. The IET process is also discussed based on density functional theory and nonequilibrium Green's function calculations. These results quantitatively reproduce many the experimentally observed features, whereas Fermi's golden rule for IETS qualitatively explains the propensity rule and site selectivity observed in the experiments. However, comparison between experiment and theory reveals a large difference in IETS intensity for the C-H stretching mode that originates from the side chains of the alkanethiol molecules. In order to explain this difference, we discuss the importance of an intermolecular tunneling process in the SAM. Application of STM-IETS to identify a hydrogenated alkanethiol molecule inserted into a deuterated alkanethiol SAM matrix is also demonstrated.

Keywords: Inelastic electron tunneling spectroscopy, scanning tunneling microscope, density functional theory, nonequilibrium Green's function, alkanethiol self-assembled monolayer, isotope labeling

Contents

1. Introduction

1.1. Alkanethiol self-assembled monolayer

Alkanethiol self-assembled monolayers (SAMs) on an Au(111) surface can be easily prepared by dipping a clean Au(111) substrate into a dilute ethanolic solution of alkanethiol [1]. The fabricated SAM is inert even under ambient conditions, which protects the Au substrate from contamination. Thus, fabricated nanodevices that use an alkanethiol SAM as a tunneling barrier retain stable electron transport properties for a relatively long period of time (more than several months) [2]. Because of these advantages, the formation processes, structures, and electron transport properties of SAMs have been intensively investigated [3–6]. The wealth of available experimental data on alkanethiol SAMs makes them benchmark materials to evaluate the validity of various theoretical approaches, including density functional theory (DFT) and nonequilibrium Green's function (NEGF) calculations [7–9].

The formation process of a SAM and its structure on an Au(111) surface have been investigated with scanning tunneling microscopy (STM) [10–15], atomic force microscopy (AFM) [16,17], and X-ray diffraction [18]. Spectroscopic methods such as X-ray photoelectron spectroscopy [19], infrared absorption spectroscopy (IRAS) [20–22], high-resolution electron energy loss spectroscopy (HR-EELS) [23–24], Raman spectroscopy (RS) [25] and metastable atom electron spectroscopy [26] have also been employed to investigate the structure and electronic properties of SAMs. These works have revealed that the alkanethiol molecules are organized by van der Waals forces between adjacent molecules to form a $(\sqrt{3} \times \sqrt{3})R30°$ structure in relation to the Au(111) substrate. In a SAM, the sulfur atoms are bound to the Au substrate and each molecule stands upright with a tilt angle of 30° [3].

The electron transport properties of alkanethiol molecules have been investigated using various junctions whereby they are located between two metallic electrodes with nanometer spacing [5]. In order to fabricate such molecular junctions, various methods have been employed, including nanopore junctions [27,28], crossed-wire junctions [29,30], and AFM [31–33], where the alkanethiol SAMs are formed on either crystalline Au(111) or amorphous Au surfaces. If a mechanical break junction [34–36] or STM [37] is employed to fabricate molecular junctions, then the number of molecules contributing to the electron transport can be tuned to just a few or even a single molecule. Changes in the substrate condition and number of molecules contributing to the electron transport process causes a difference to the absolute value of the conductivity; however, all papers have reported that there is an exponential relationship between the resistivity and length of the molecules, with a decay constant of ca. 1 $Å^{-1}$ [5,27,31,32].

In order to understand the reported conductivity of alkanethiol SAMs or molecules, characterization of the molecules in the nanoscale region is essential, where the electrons actually tunnel. With this purpose in mind, adaption of conventional spectroscopic methods such as IRAS and HREELS to the molecular junction is difficult because of the spatial resolution. Conventional characterization methods require a minimum of 10^{12} molecules to obtain sufficiently intense vibrational signals [38], i.e., the acquired information is the average of many molecules in the macroscopic region. In contrast, inelastic electron tunneling spectroscopy (IETS) can be adopted for even a

single molecule. In this article, we review the recent progress that has been made on the use of IETS for alkanethiol SAMs, where IETS is compared to alternative, more conventional vibrational spectroscopy techniques [39–43]. IET spectra obtained for various junctions are also compared and the propensity rule of IETS is discussed using state-of-the-art theory based on DFT and NEGF [9,44,45].

1.2. HREELS for an alkanethiol SAM

Vibrational spectroscopy, such as IRAS and HR-EELS, is a powerful method for chemically analyzing molecules that are adsorbed on surfaces. For example, the investigation of vibrational modes with energies between a few tens of meV to 200 meV provides information inherent to the molecules in question. These modes can be used to identify the molecules investigated, thus they are called modes in the fingerprint region. The selection rules of IRAS are well known, with the vibrational modes corresponding to changes in the dipole moment perpendicular to the surface normal showing strong peaks [46]. In the case of dipole scattering in EELS, the same selection rules as IRAS can be adopted [46]. Through this dipole active selection rule, vibrational spectroscopy can provide information not on only the chemical composition, but also on the geometrical structure of the molecule.

Vibrational features of an alkanethiol SAM have been thoroughly investigated by Kato et al. using HREELS [23]. They prepared alkanethiol SAMs on Au(111) surfaces with various lengths of alkanethiol molecules ($CH_3(CH_2)_{n-1}S$/Au(111), $2 \leq n \leq 18$). With their sample preparation, they could fabricate a SAM with large, well-ordered domains. By virtue of this sample property, they were able to obtain decent EELS signals from the dipole scattering. Experimentally observed signals with prominent intensities result from the CH_2 rocking mode at 89 meV, the CH_3 s-deformation mode at 171 meV, and the CH_3 d-deformation or CH_2 scissor modes at 180 meV (see Fig. 1). Besides these large signals, many other vibrational modes were detected, including Au-S stretching modes at 28 and 32 meV, a CH_3 rocking mode at 113 meV, a C-C stretching mode at 130 meV, and a CH_2 twist mode at 157 meV.

Among these detected signals, the CH_3 s-deformation mode with the energy of 171 meV shows a strong even-odd effect on the number of carbon atoms that constitutes the alkyl chain (see Fig. 1), i.e., when it is even this signal becomes strong and when it is odd this signal becomes weak. This result is consistent with the geometrical structure of the alkanethiol SAM shown in the inset of Fig. 1. In the case of the even number, the terminal methyl group is pointed in the direction perpendicular to the surface. Thus, the change in dipole moment perpendicular to the surface is large, providing strong dipole scattering. On the other hand, in the case of an odd carbon number, the terminal methyl group points in a parallel direction to the surface, resulting in a smaller change in the dipole moment perpendicular to the surface and less probability of dipole scattering.

Kato et al. also investigated impact scattering for alkanethiol SAMs with EELS, where the vibrational signals prominent by dipole scattering, such as the CH_2 rocking mode at 89 meV, the CH_3 s-deformation mode at 171 meV, and the CH_3 d-deformation or CH_2 scissor mode at 180 meV, are decreased and become comparable to the peak intensity of the C-C stretching signal at 130 meV (see the dotted lines in Fig. 1). In other words, the selection rules for impact scattering are more relaxed than those for dipole scattering are.

The even-odd effect of an alkanethiol SAM is also observed in IRAS for the C-H stretching mode of the terminal methyl group [21]. As mentioned above, the terminal methyl group points in a perpendicular direction when the carbon number is even. In this case, the change in dipole moment originating from the symmetric stretch of the methyl group is larger than that in the case of an odd carbon number. Thus, the strong C-H symmetric stretching signal is detected in the case of an even carbon number, but not when there is an odd number of carbons.

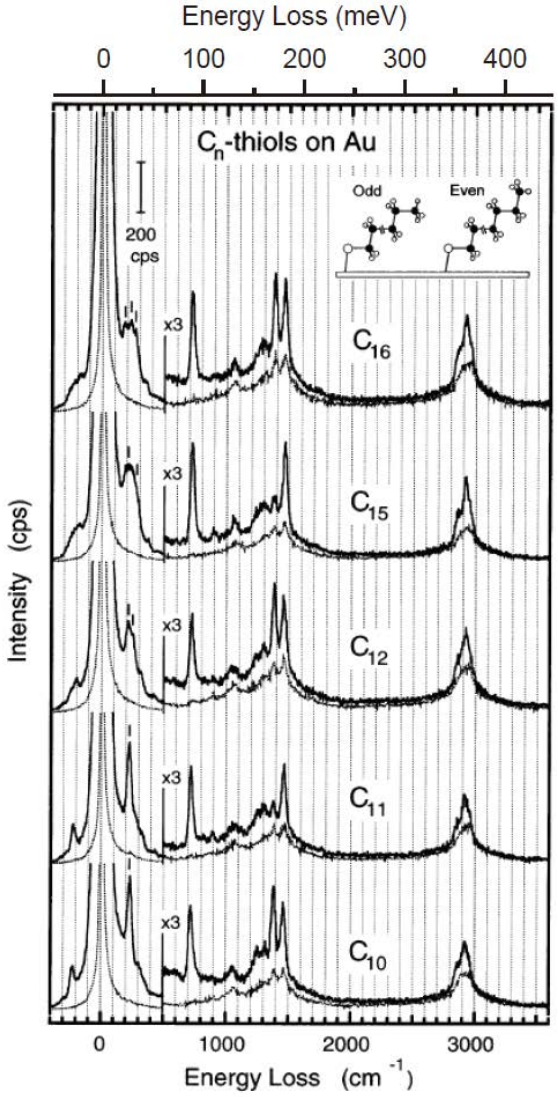

Fig. 1. HREEL spectra for various alkanethiol (C_n-thiol) SAMs on Au. The solid and dotted lines correspond to specular spectra detected at 60° and off-specular spectra detected at 42°, respectively. The inset shows schematic models of an alkanethiol SAM structure for an odd and even number of carbons [23].

1.3. Inelastic electron tunneling spectroscopy

In contrast to IRAS and HR-EELS, IETS has advantageous spatial resolution, i.e., IETS is capable of detecting even a single molecule [47–49]. A schematic view of the IETS process is shown in Fig. 2, where we assume that the density of states of the sample and tip are independent of the electron energy. The tunneling process between the tip and substrate can be divided into two processes: elastic electron tunneling (Fig. 2(b)) and inelastic electron tunneling (Fig. 2(c)). In the former process, electrons tunnel without losing their initial energy, while in the latter process the electrons tunnel and lose their energy by exciting the vibrational modes of the molecule that constitutes the tunneling junction. In the case of elastic tunneling, the current increases linearly with an increase in the sample bias, if one assumes a constant tunneling matrix element for the sample bias. When the increased sample bias is achieved for a certain vibrational energy ($h\nu$) of the molecule, the inelastic tunneling process exciting the vibrational mode of the molecule is opened up, where h is Planck's constant, ν is the vibrational frequency, and e is the elementary charge. This inelastic process appears as a change in the slope of the I vs V (Fig. 2(d) or Fig. 2(g)), as a step in the dI/dV vs V (Fig. 2(e) or Fig. 2(h)), and as a peak or dip in the d^2I/dV^2 vs V (Fig. 2(f) or Fig. 2(i)). Whether the peak or dip is observed in the d^2I/dV^2 vs V depends on transmission through a molecule and ratio of a molecular coupling to two electrodes (see Section 1.3 and 2.2) [50].

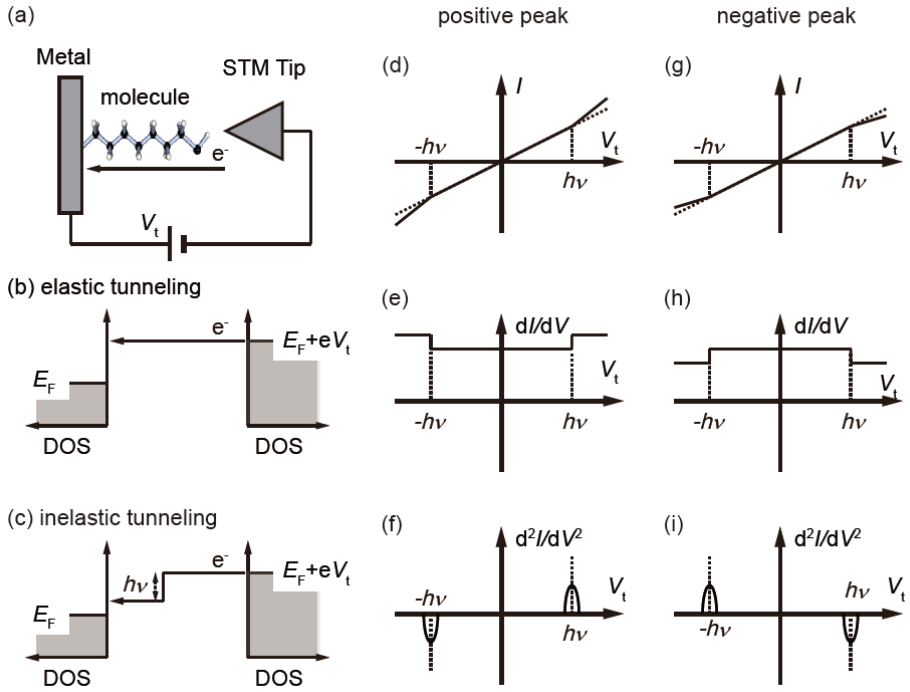

Fig. 2. Schematic view of (a) the tunneling process through a molecule on the surface, (b) elastic and (c) inelastic tunneling processes. (d)–(f) show the effect of the inelastic process on the I vs V, dI/dV vs V, and d^2I/dV^2 vs V, respectively, where the inelastic current is increased with increasing the bias V_t. (g)–(i) are similar to (d)–(f), however, here the inelastic current is decreased with increasing the bias.

IETS was first investigated by Jacklevic and Lambe, who examined a macroscopic tunneling junction and structure of a metal-insulator-molecule-metal [51]. Since then, much IETS data has been accumulated [52–54] due to its advantage of high sensitivity. Taking into account the fact that the IET spectrum for a macroscopic tunneling junction is an average of the many interactions between electrons and vibrational modes of the molecules, proposed models for the IET process have been based on long-range interactions such as electron-dipole interaction [55] and electron-induced diploe interaction [56]. Following these pioneering works, IETS was drastically improved through the use of STM.

IETS studies using STM (STM-IETS) were first investigated by the group of Ho [57]. Since then, many papers on IETS and the inelastic electron induced dynamics of molecules have been reported for single molecules on metal surfaces [58–73]. For example, the C-H stretching signal was preferentially detected for an acetylene molecule on a Cu(100) surface, where the spatial distribution of the IET signal was found to be localized near the molecule [70]. In addition to hydrocarbon molecules, vibrational modes of simple molecules such as CO and O_2 on metal surfaces have also been reported using STM with atomic spatial resolution [71–73]. Following these experimental findings, theory has progressed based on the short-range interactions between the tunneling electrons and the vibrational mode [74–80]. State-of-the-art theory was able to reproduce the features observed by experiment, for example, preferential observation of C-H stretching signal for acetylene molecules [74]. IETS works closely related to surface science have since been extended to those related to molecular electronics [7–9,28,36,81–108], owing to the expectation for molecular electronics as a post-silicon technology.

1.4. Examples of IETS

Examples of experimental IET spectra for four different kind of samples are shown in Fig. 3 by blue lines: (a) an oligophenylenethynylene (OPE) molecule connected to two gold electrodes by chemisorption [81], (b) a gold chain connected to two gold electrodes [109], (c) an O_2 molecule on an Ag(110) surface investigated with an STM [73], (d) a CO molecule chemisorbed on a Cu(111) surface investigated with an STM [110]. In the case of (a) the OPE and (d) the CO molecule, the peaks are observed at the positive bias in the d^2I/dV^2 vs V, on the other hand, for (b) the gold chain and (c) the O_2 molecule the dips are observed in the positive bias.

These observations can be interpreted by a model assuming a one-level contributing to an electron transfer, where the electron transfer is considered in terms of the ratio of molecular coupling to two electrodes (α) and transmission (τ) [50]. According to this model, the maximum transmission is described by $\tau_{max}=4\alpha/(1+\alpha)^2$ (see the thick line in Fig. 4) and a crossover point, where the peak in the d^2I/dV^2 is changed to the dip, is described by $\tau_{crossover}=\tau_{max}/2$ (see the red dashed line in Fig. 4). This diagram means that for a given coupling ratio, if the transmission is higher than the critical value (half of its maximum), the inelastic back scattering prevails over the inelastic forward scattering, leading to the decreased tunneling probability.

The four samples treated here are located in the phase diagram as follows. (a) The OPE molecule is connected similarly to the two electrodes via strong chemical bond

(α~1) and the one-level is far from the Fermi level (τ~0). Thus the OPE is located above left in the phase diagram, which provides the peaks in the d^2I/dV^2 vs V at the positive bias. (b) The gold chain is also connected strongly and symmetrically to the two electrodes (α~1), however, the transmission is higher than the half of the maximum; the position is above right in the phase diagram, providing the dips. Both of the (c) O_2 and (d) CO molecule are investigated by STM, thus the coupling is anti-symmetric (α~0). On the other hand, the transmissions are considerably different between the CO and O_2 molecule, i.e, the CO shows off-resonant tunneling and the O_2 shows resonant tunneling. By this contrast, the CO is located in the left side of the cross over line (providing the peaks) and the O_2 is located in the right side of the cross over line (providing the dips) [50]. Besides this qualitative consistence between the experiments and theory, numerical calculations based on DFT and NEGF (see Chapter 2) quantitatively well reproduce the experimental observations (see black lines in Fig. 3) [50].

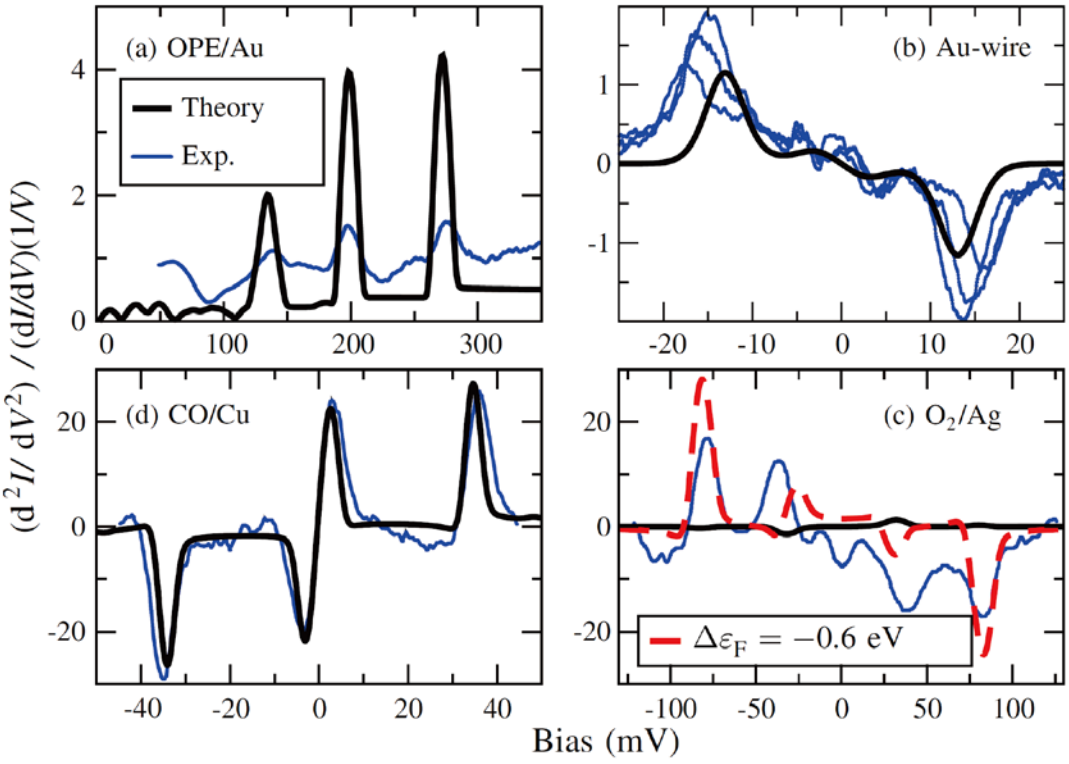

Fig. 3. Experimental (blue lines) and Calculated (black lines) IETS for (a) OPE molecule with Au(111) leads [81], (b) Au chain connected to Au(100) leads [109], (c) O_2 molecule on Ag(110) [73], and (d) CO molecule on Cu(111) [110]. In case (c), Fermi energy in the calculation has been shifted manually to match the experiment (red dashed line). The calculation data originate from Ref. [50]. For the STM configurations (c) and (d), the calculated IETS is compared with a rescaled d^2I/dV^2 [50].

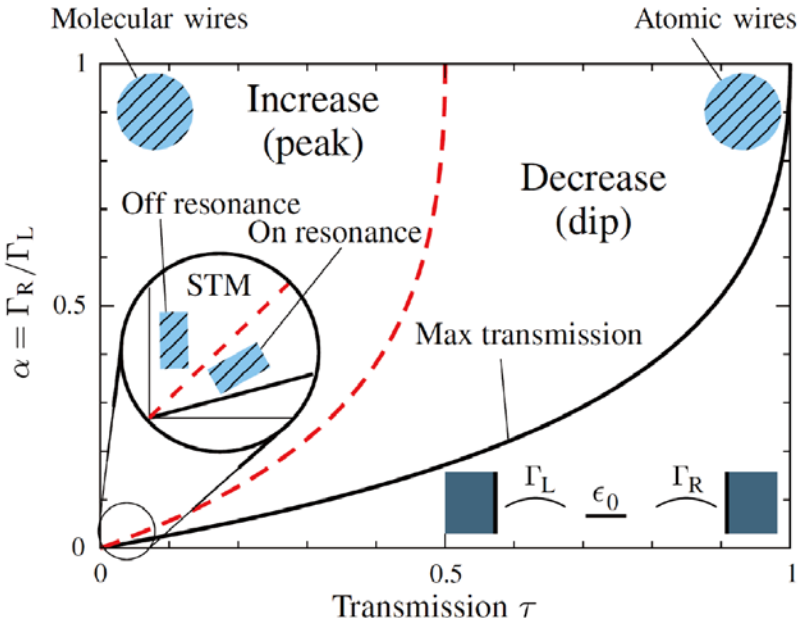

Fig. 4. Phase diagram for a one-level model. The inset illustrates the sign of the conductance change at the onset of inelastic tunneling. At a given coupling ratio, the elastic transmission has an upper bound max (thick line), and the inelastic conductance change undergoes a sign change at crossover $\tau_{crossover}=\tau_{max}/2$ (red dashed line).

1.5. IETS for alkanethiol SAMs

Alkanethiol SAMs are a prototype sample in molecular electronics, whose IETS was first independently investigated by the groups of Reed [28] and Kushmerick [81]. The former group adopted a nanopore junction where the alkanethiol SAM was formed on the gold electrode in the nanopore and the counter electrode was fabricated by evaporation of the gold on the top of the SAM film. On the other hand, the latter group employed a crossed-wire junction, where the gold wire (diameter of 10 μm) coated by the alkanethiol molecule was intersected by another gold wire with the same diameter but without the alkanethiol SAM. The distance between the first and second wires can be tuned by the Lorentz force produced by the magnetic field and the current passing through the wire [29,30]. By this method, it is possible to produce the condition where electrons can tunnel from one gold wire to another. Similar alkanethiol molecules were employed in both reports; however, the results of the IETS showed large discrepancies (see Fig. 5).

The origin of this IETS discrepancy was investigated by the group of Kushmerick, who adopted crossed-wire junctions and measured IETS for two types of samples: multilayer molecular junctions with and without incorporation of metal nanoparticles [111]. When the sample with incorporated metal particles was measured, a simple peak shape is observed in its IETS owing to the off resonant tunneling condition. On the other hand, when IETS for the metal incorporated sample was measured, peaks with derivative line shape were found owing to the resonant tunneling process. This derivative shape found in the metal-incorporated sample was similar to the experimental

result reported for the alkanethiol molecules in the nanopore junctions [28]. Thus Kushmerick et al. suggested the possibility that the nanopore devices contained nanoscale metal islands in the alkanethiol molecules due to the deposition process of top electrodes.

This interpretation on the IETS discrepancy depending on the junction type seems to be reasonable, because Persson and Baratoff theoretically predicted the change of IETS features depending on the on/off tunneling condition [112] and their prediction was consistent with the interpretation by Kushmerick et al. [111]. Besides this interpretation, a straightforward investigation to understand the discrepancy (standardization of the IETS data) is still required, allowing for the fact that alkanethiol molecules are benchmark materials for molecular electronics. In order to obtain such standard data, IETS with STM is very effective, as with the case of the surface science-related research described above, because STM-IETS can confirm whether a well-ordered structure is formed or not. In addition, by virtue of the finite controllability of the tip position with respect to the molecule, it is possible to tune the contact condition between the tip and molecule.

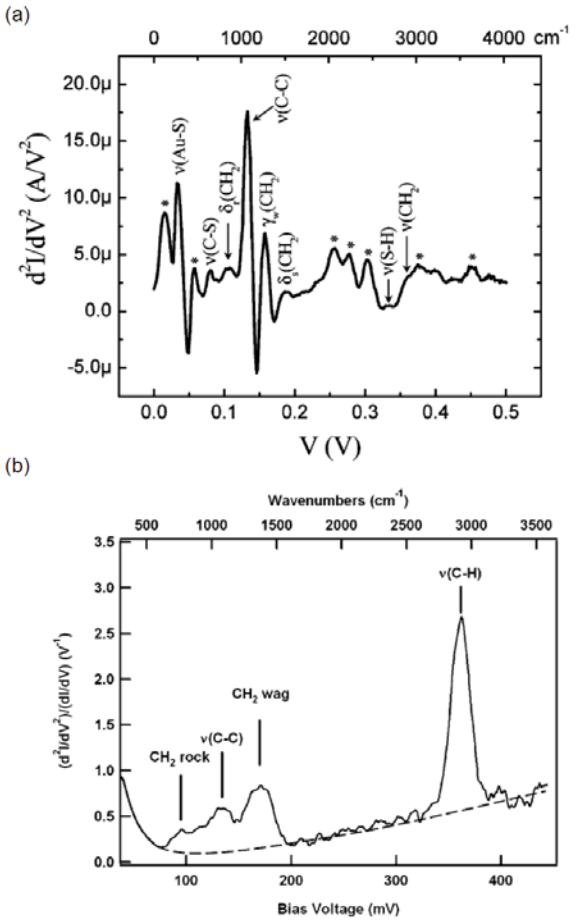

Fig. 5. IET spectra of (a) an octanedithiol ($HS(CH_2)_8SH$) SAM using a nanopore junction [28] and (b) an undecanethiol ($CH_3(CH_2)_{10}SH$) SAM using a crossed-wire junction [81].

1.6. Surface enhanced Raman spectroscopy

Finally in this chapter, we would like to comment on Raman spectroscopy (RS), which provides vibrational information of macroscopic number of molecules adsorbed on a surface as in the case of HR-EELS and IRAS. By measuring RS, we can obtain information on molecular conformation such that the ratio of trans-structure of alkyl chain to gauche-structure in alkanethiol SAM surfaces [25]. The Raman intensity can be enhanced by putting molecules in a nanoscale region between two metal electrodes, owing to the increased electromagnetic field, which is called surface enhanced RS (SERS). By virtue of this intensity enhancement, SERS can be adopted even for a single molecule [113-115]. Combining the SERS with STM can be a characterization method simultaneously acquiring both of microscopic and vibrational information as in the case of the STM-IETS [114]. The advantage of SERS is that this method can be adopted while measuring a tunneling current passing through a molecule. For a metal-molecule-metal junction, a bias applied to the molecule sometimes changes the conformation of the molecule, which can be directly detected by SERS [115]. Besides this point, SERS can be adopted even at room temperature, which means that SERS is more widely applicable than STM-IETS requiring very low temperature (~4 K). On the contrary, spatial resolution of SERS is still 15 nm [114], which is one order of magnitude larger than that of STM-IETS [47].

2. Theory of IETS

2.1. Methods to calculate IETS

The main methods used to theoretically calculate IET spectra from DFT are based the NEGF method [45,74,112] which is able to predict both increases and decreases of the conductance. Using further approximations limits the theory to predict either increases or decreases in the conductance [8,45,104]. These approximations have the advantage of giving equations which are easy to interpret as scattering theory. The advantages of this scattering theory are that it is computationally tractable and gives physical insights into the scattering processes. However, note that application of the approximate scattering theory does not reveal whether the electron is backscattered or forward scattered, and disregards corrections due to the elastic conductance. It is thus only applicable to systems where the inelastic scattering either increases or decreases the current. NEGF methods on the other hand correctly describe the corrections to the elastic current and can describe experiments where the current is increased and/or decreased due to the inelastic scattering giving rise to peaks and/or dips in the second derivative. The main disadvantages of the NEGF method are that without approximations the method is computationally very expensive and the results difficult to interpret.

We have recently developed the Lowest Order Expansion (LOE) approximation of the NEGF method which makes it computationally feasible to calculate the IETS from large scale DFT calculations [45,50]. In addition, the LOE equation for the rate of emission is identical to Fermi's golden rule expression. The LOE is therefore suited to provide physical insights of the scattering processes and selections rules for IETS from first principle calculations.

2.2. Lowest order expansion

The LOE approximation is based on the NEGF method to describe the electron transport problem coupled to localized vibrations. NEGF gives clear prescriptions of how the current through the junction and the power delivered to the vibrations from the tunneling electrons are to be calculated. To simplify these expressions we utilize two approximations. First we expand the expressions of the current and power to the lowest order in e-ph coupling. Additionally, the density of states is assumed to be slowly varying near the Fermi level. In this case, the integration over energy can be carried out analytically and only a few terms remain.

Using the low temperature limit to simplify the presentation, the expression for the power dissipated from the electrons into the vibrational system is given in the LOE approximation by

$$P = \sum_{\lambda} \frac{(\hbar\omega)^2}{\pi\hbar}\left(n_B(\hbar\omega) - n_\lambda\right) Tr\left[M_\lambda A M_\lambda A\right] + \frac{\hbar\omega}{e}\gamma_\lambda \begin{cases} 0 & ;|eV| < \hbar\omega \\ |eV| - \hbar\omega & ;|eV| > \hbar\omega \end{cases} \tag{1}$$

where $\hbar\omega$ is the vibrational energy, $n_B(\hbar\omega)$ the Bose-Einstein distribution, n_λ the actual occupation of the vibrational mode, M_λ the e-ph interaction, A the spectral function, and γ_λ the emission rate discussed below [45]. The first term drives the vibrational system towards equilibrium with the electrons since it is the electronic temperature which enters the Bose-Einstein distribution. The second term describes vibrational heating where the emission rate is given by

$$\gamma_\lambda = \frac{e}{\pi\hbar} Tr\left[M_\lambda A_L M_\lambda A_R\right] = \frac{4\pi e}{\hbar}\sum_{l,r}\left|\langle \Psi_r | M_\lambda | \Psi_l \rangle\right|^2 \tag{2}$$

where A_L, A_R are the spectral functions of the two leads connecting the scattering region. The scattering rate can further be rewritten in terms of the scattering states incoming from the two leads ($|\Psi_r\rangle$ or $|\Psi_l\rangle$). The equation thereby resembles Fermi's golden rule and if the scattering states are known, selection rules based on the symmetry of the scattering states and e-ph coupling can be derived.

In most cases, the electrons emitting vibrations will either be forward scattered and contribute to the current (peak in IETS) or backscattered (dip in IETS). The change in current is therefore approximately the electron charge times the rate of scattering events which can be found from Eq. (2). The crossover from peak to dip in simplified models occurs at a transmission of 1/2 [50]. Although these simplifications seem to be correct for most systems we have studied, in the actual calculation of the IETS we use the LOE expression for the current instead

$$\begin{aligned} G^{LOE} &= G_0\tau + \sum_\lambda e\gamma_\lambda^{LOE}\theta\left(|eV| - \hbar\omega\right) + G_\lambda^{Asym} \\ \gamma_\lambda^{LOE} &= \frac{e}{\pi\hbar} Tr\left[G^+\Gamma_L G\left\{M_\lambda G\Gamma_R G^+ M_\lambda + \frac{i}{2}\left(\Gamma_R G^+ M_\lambda A M_\lambda - h.c.\right)\right\}\right] \end{aligned} \tag{3}$$

where G_0 is the conductance quantum, τ the transmission, G, G^+ and Γ_L/Γ_R the retarded, advanced Green's functions and broadening by the leads. In addition to the elastic conductance (first term), the LOE expression gives a step in the conductance at the vibrational energy (second term). The last term, G_λ^{Asym}, is an asymmetric term that is usually small and will be ignored in the following. The LOE current scattering rate, γ_λ^{LOE}, can give peaks and/or dips in the IETS since the LOE approximation correctly accounts for the inelastic current and the change in elastic conductance. However, compared to the power, the rate is more difficult to analyze in terms of scattering states.

2.3. DFT calculations of octanethiol IETS

To calculate the IETS using DFT and the LOE approximation, the e-ph coupling matrices M_λ, phonon energies, and various Green's functions need to be computed from DFT. Using the TranSIESTA [116–118] software, we have previously developed methods to accomplish these tasks [9,50]. The phonon energies and e-ph coupling were calculated by a finite difference approach where each atom of the molecules was displaced in three directions. The Green's functions were found from elastic transmission calculations by attaching semi-infinite leads to the scattering region.

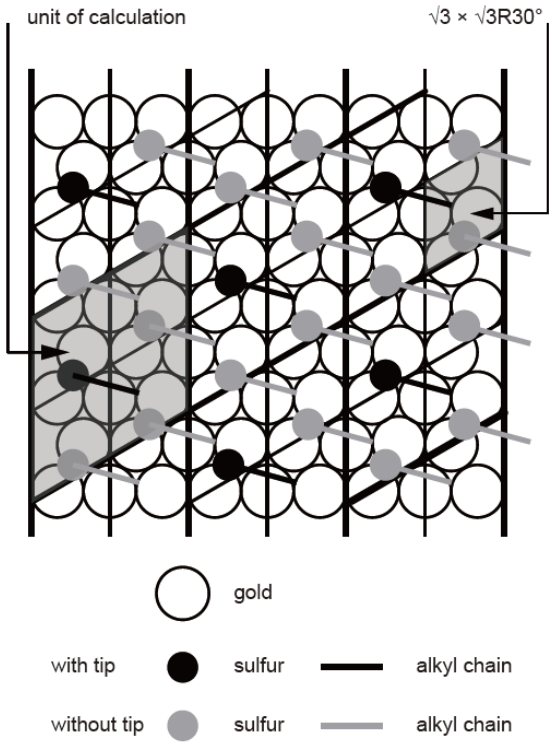

Fig. 6. Schematic showing an octanethiol SAM on Au(111). The unit cell used in the IETS calculation is shown by thick black lines. The STM tip modeled by one protruding Au atom was placed approximately over the end group of the octanethiol whose alkyl chain and sulfur atom are depicted in black (gray for without the tip).

Calculations of the octanethiol IETS were performed by first optimizing the geometry of the $\sqrt{3} \times \sqrt{3}R30°$ SAM structure on a Au(111) slab (see Fig. 6). The stable geometry was found to have the sulfur atom on the bridge site of the gold surface. This geometry was repeated to give a unit cell containing four molecules (2 × 2). The STM tip was simulated using one Au atom protruding from the Au(111) slab with a tip-C distance of 3.3 Å. Using periodic boundary conditions both the substrate and tip were modeled using the same Au(111) slab. Because of the periodic boundary conditions, the tip atom was not centered directly above one of the molecules but displaced by 1.2 Å, along the surface, from the center of the CH_3 end group. Vibrational energies and the e-ph coupling were thereafter obtained from a finite difference scheme [45]. The IETS itself was calculated using the lowest order expansion (LOE) method by combining the e-ph coupling with the Green's functions calculated using TranSIESTA. To simulate the broadening of the IETS, temperature broadening and the experimentally used lock-in modulation voltage broadening were included. In the case of octanethiol SAM, the LOE approximations are well justified since less than 3% of the electrons undergo inelastic scattering [39], and the conductance is almost bias independent (see Section 4.3)[39].

2.4. Theoretical analysis of the calculations

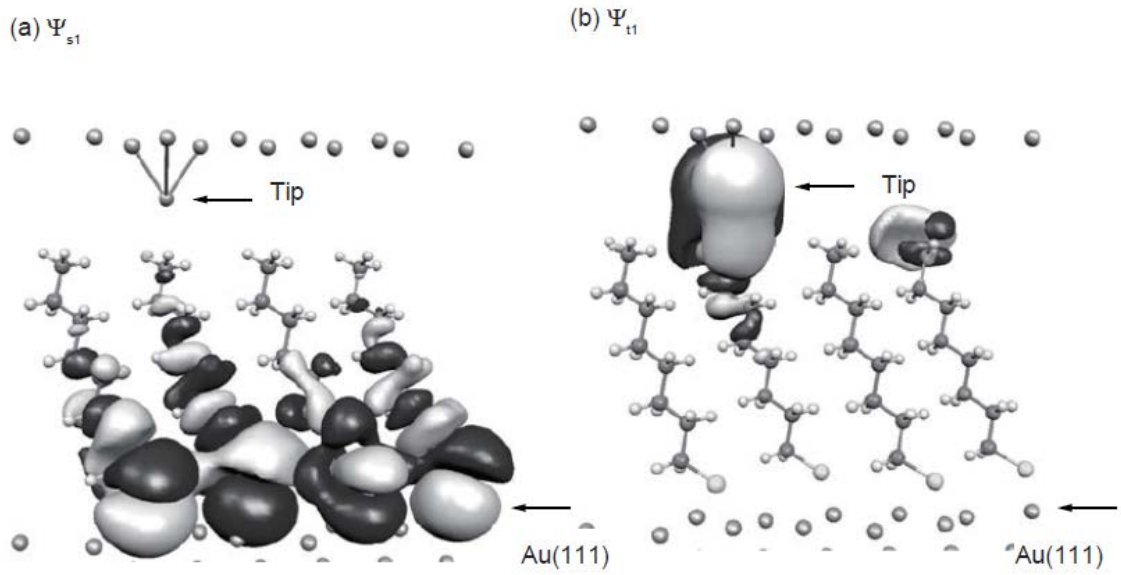

Fig. 7. Scattering states at the Fermi level. Maximally transmitting scattering states (eigenchannels) incident from (a) substrate side and (b) tip side. The color (black/white) of the isosurface plots indicate the sign of the scattering state [41].

The results of DFT calculations can be difficult to interpret especially if a physical insight of the scattering processes is not present. To understand and interpret the results of the calculations we have therefore developed methods to analyze the IETS in term of scattering states and to visualize the elastic and inelastic current traversing the molecule. From the expression of the vibration emission rate, Eq. (2)**,** we are able to write the scattering rate as a sum of initial and final scattering states as follows:

$$I_{inel} \propto \sum_{l,r} \left| \langle \Psi_r | M_\lambda | \Psi_l \rangle \right|^2 \tag{4}$$

However, since there are several scattering states incident from the substrate, we utilize the so called eigen-channels [119], i.e., maximally transmitting scattering states. In practice this means that the majority of the scattering rate in Eq. (4) is given by the first eigen-channels. We can therefore find approximate selection rules (propensity rules) based on the first term of Eq. (1) [50].

The maximally transmitting eigen-channels for the octanethiol SAM are shown in Fig. 7. They have the largest amplitude throughout the molecule and therefore largest matrix element between tip/substrate scattering states [119]. Both eigen-channels have a σ-type symmetry originating from C-C bonds, which is exponentially decreasing as the electrons tunnel through the molecule. In the following section, we will compare the experimental results with the theoretical calculations and qualitatively discuss the features of the experiment by using Fermi's golden rule.

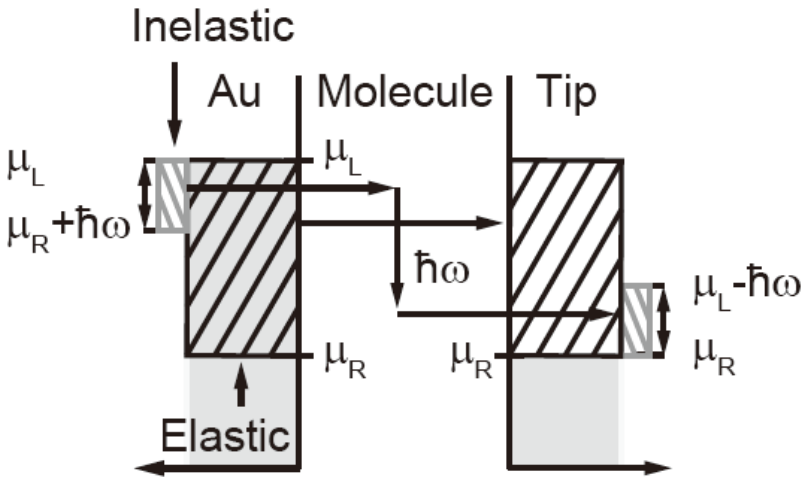

Fig. 8. Energy phase space available for elastic and inelastic scattering.

In addition to the eigen-channel scattering states we also analyze the conduction path for the elastic and inelastic current by plotting the energy resolved current density (see Section 5.5). These current densities were calculated from the energy resolution of the density matrix (ρ) given by

$$\rho = \frac{1}{2\pi} \int G\Gamma_L G^+ f_L(\varepsilon) + G\Gamma_R G^+ f_R(\varepsilon)\, d\varepsilon \tag{5}$$

where the Fermi-functions of the two leads ($f_L(\varepsilon)$ and $f_R(\varepsilon)$) specify the occupation of the scattering states. In the low temperature limit, assuming the chemical potential of the leads $\mu_L > \mu_R$, the density matrix in the energy range between μ_L and μ_R, is simply given

by $G\Gamma_L G^+$. From the density matrix, the current density was calculated from the current operator and summed over basis orbitals corresponding to different atoms.

The changes in the density matrix due to the e-ph coupling were thereafter calculated using the LOE approximations. This leads to a decrease in the density from out-scattering of electrons in the high energy region between μ_L and μ_R,+ħω where an empty final state is available (> μ_R) (see Fig. 8). The in-scattering of electrons similarly increase the density in the energy range between μ_L- ħω and μ_R. The corresponding changes to the energy resolved current densities can thereafter be plotted showing the effects of in- and out-scattering on the current densities.

3.3. Experimental methods of STM-IETS for an alkanethiol SAM

3.1. STM system

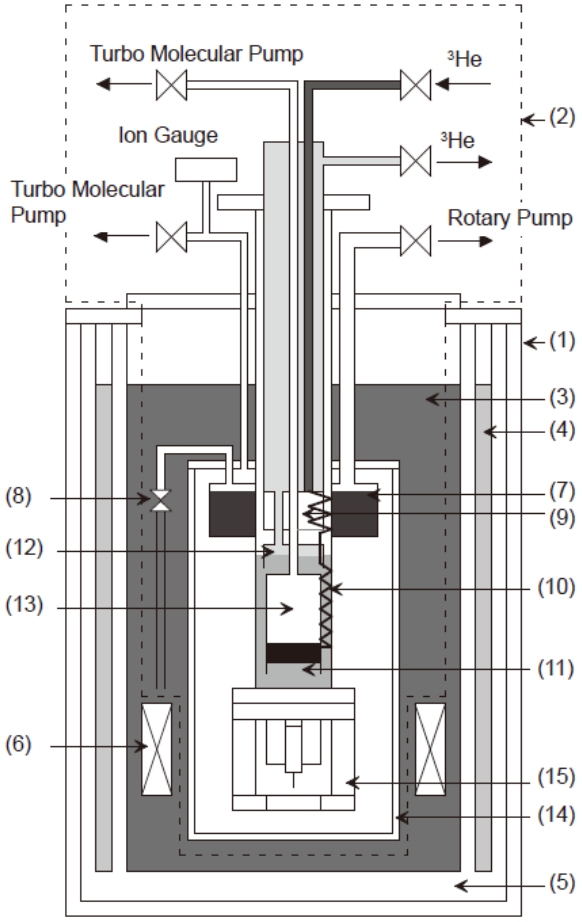

Fig. 9. Schematic of a compact ultra-low temperature STM system. (1) Cryostat, (2) dilution refrigerator-based STM, (3) liquid helium bath, (4) liquid nitrogen bath, (5) vacuum thermal shield, (6) 5 T magnet, (7) 1 K pot, (8) needle valve, (9) ^{3}He condenser, (10) heat exchanger, (11) mixing chamber, (12) still, (13) plunger, (14) vacuum chamber, and (15) STM head. The cryostat is mounted on a vibration-isolation table (not shown) [40].

The STM system used is based on (1) a dilution refrigerator-type STM and (2) a liquid helium cryostat (see Fig. 9) [40]. The cryostat and dilution refrigerator (TC330-SCM and TS-3H100, Taiyo Nissan, Japan), and the STM unit (USSS-9990, Unisoku, Japan) are all commercially available. The cryostat consists of (3) a 57 L liquid helium bath, (4) a 26 L liquid nitrogen bath, (5) a vacuum thermal shield, and (6) a 5 T superconducting electromagnet. The cryostat is mounted on a vibration-isolation table (AWF-1510DTU, Meiritsu Seiki Co., Japan), which is not shown in the figure. By using this setup and operating the dilution refrigerator, we can acquire IET spectra at a temperature of 260 mK [40]. However, for the vibrational spectroscopy of alkanethiol molecules the resolution of the spectra at 260 mK showed no improvement over those obtained at 4.4 K because of other experimental factors for the present case (see Section 4.5). Thus, we omit details on the operation principles of the dilution refrigerator [40]. This system is used by simple cooling with liquid He and once the liquid He is filled to full volume, the STM can be operated at a stable temperature of 4.4 K for 2–3 day without requiring a further supply of liquid He.

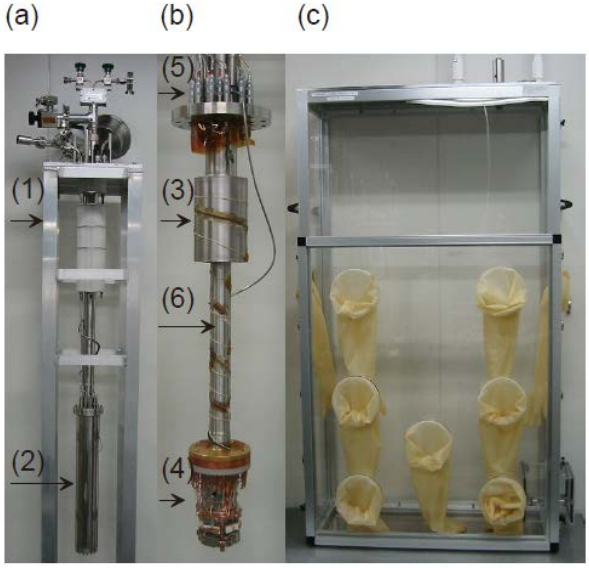

Fig. 10. Photographs of (a) the dilution refrigerator-based STM, (b) the inner structure of the vacuum chamber, and (c) the custom-made glove box. (1) Support table, (2) vacuum chamber, (3) 1 K pot, (4) STM head, (5) feed-through, and (6) circular cylinder. The ^{3}He condenser, heat exchanger, mixing chamber, still, and plunger are contained inside the circular cylinder [40].

The dilution refrigerator-based STM (Fig. 10(a)) can be removed from the cryostat and mounted on a custom-made glove box (Izumitec, Japan) that is equipped with an oxygen meter, a moisture analyzer, and a pass box (Fig. 10(c)). A sample can be transferred from the bottom of the STM unit (Fig. 10(b)) in an inert gas atmosphere. After transferring the sample, the vacuum chamber, which is sealed (also in an inert gas condition), can again be moved to the cryostat. Thereafter, the vacuum chamber is evacuated by a turbo molecular pump (TMP) for 1 day. The operation of the TMP is discontinued once the bath is filled with liquid He. When the vacuum chamber reaches

its minimum temperature, the wall of the chamber is expected to work as a cryogenic pump. The ion gauge (see Fig. 9) that is connected to the vacuum chamber via a narrow tube shows pressures in the range of 10^{-8} Torr. This pressure is achieved due to the low conductance of the narrow tube, and we believe that a lower pressure is achieved near the STM head.

The coarse motion of the STM is operated using a slip and stick motion, where the maximum movement of the *XY* stage is ±0.5 mm. The maximum scan area of the STM piezo tube for *XY* is 3.4 × 3.4 μm^2 at 300 K and 1.0 × 1.0 μm^2 below 4.4 K. The coarse motion and scanning of the STM is controlled by commercially available units (PMC100 and SPM100, RHK, USA) and operated using their accompanied software (XPM, RHK, USA).

3.2. IETS and its mapping method

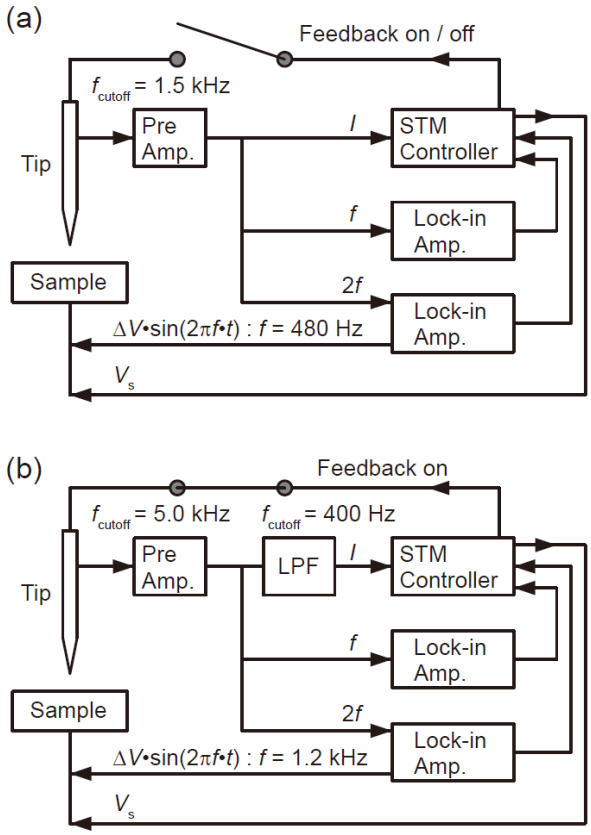

Fig. 11. Schematic drawing of (a) a conventional IETS measurement system and (b) an improved mapping system for the IET signal [43].

The inelastic signal originating from a vibrational mode with energy $h\nu$ appears as a step-like feature at the sample bias of $h\nu/e$ in the dI/dV curve and a peak or a dip at the sample bias of $h\nu/e$ in the d^2I/dV^2 curve. Use of a lock-in amplifier is effective for obtaining high-precision dI/dV and d^2I/dV^2 curves. A schematic of the IETS measurement system is shown in Fig. 11(a), where the modulation voltage ($\Delta V\sin(2\pi ft)$) is applied to the sample bias (V). In this case, the tunneling current (I) can be

approximated as follows:

$$I(V + \Delta V \sin(2\pi ft)) \approx$$
$$I(V) + \frac{dI}{dV}\Delta V \sin(2\pi ft) + \frac{d^2 I}{dV^2}\frac{(\Delta V)^2}{4}\sin(4\pi ft - \frac{\pi}{2}) + \frac{d^2 I}{dV^2}\frac{(\Delta V)^2}{4} \quad . \qquad (6)$$

Hence, dI/dV can be obtained by detecting the AC current modulated at f, and d^2I/dV^2 can be obtained by detecting the AC component modulated at 2f where the phase of the modulation current is delayed by −90° compared to that of the modulation voltage. The modulation frequency was set to 480 Hz and the cutoff frequency of the pre-amplifier was set to 1.5 kHz. The tunneling current was converted to a voltage signal by a pre-amplifier (IVP-PGA and IVP-200, RHK, USA), which was then divided into two paths: one is to an input of an STM controller (SPM100, RHK, USA), for gap control, and the other is input to a lock-in amplifier (NF5640, NF corp., Japan), for the conductance and the IET signal measurement. The output of the lock-in amplifier was recorded using an STM controller (see Fig. 11(a)).

It is noted that in the actual experiment the phase shift between the modulation voltage and output modulation current resulting from the STM system should be accounted for, particularly from the preamplifier. The phase shift due to the STM system is determined as follows. First, the STM tip is retracted by a few tens of nm from the surface to a point where the tunneling current cannot be detected. Next, a modulation bias with frequency f is applied to the sample, producing an AC current (displacement current) with frequency f. This AC current is produced solely due to the capacitance between the tip and sample. By maximizing the magnitude of the AC current using the lock-in amplifier, the phase shift between the input modulation voltage and output modulation current can be determined. The phase shift for the frequency 2f can also be estimated by repeating the same procedure. The phase shift due to the STM system is stable, it is therefore not necessary to repeat the phase determination process once it has been determined.

Mapping of IET signals is an effective method for visualizing the distribution of molecular species on a surface [110,120]. Sainoo et al. reported on a mapping method of IET signals using a conventional measurement system (Fig. 11(a)), where the feedback loop was activated during the mapping process [121]. In order to minimize the effect of the modulation voltage on the feedback loop, they employed a high-frequency modulation voltage and a low time constant on the feedback loop. However, the restriction of the time constant on the feedback loop and remnant effects of the modulation voltage on the feedback system prevent a good topographic image and IETS mapping from being obtained for a high tunneling resistance sample like alkanethiol SAMs. Actually, in our mapping experiment using the same set-up, we could not obtain satisfactory IET mapping for a hexanethiol SAM.

In order to solve this problem, we minimized the AC component of the tunneling current signal that is used for controlling the tunneling gap [43]. This was achieved by inserting a low-pass filter (3314, NF Corp., Japan) between the pre-amplifier and STM controller (see Fig. 11(b)), which results in a reduction of the feedback response by the modulation voltage. We set the modulation frequency at 1.2 kHz, the cutoff frequency of the pre-amplifier at 5 kHz and the cutoff frequency of the low-pass filter at 400 Hz. The attenuation slope of the low-pass filter was 48 dB/oct, making the transmission rate

of the modulation current at 1.2 kHz to be less than 0.1%. Under this condition, we could see no change in the modulation current for frequency *f* at the input of the lock-in amplifier, with or without the feedback loop engaged.

3.3. Sample preparation

An SAM film of alkanethiol was formed by following established methods [3]. First, the Au/mica sample (MI, USA) was annealed in air using a hydrogen torch. Immediately upon annealing, the sample was immersed in an ethanol solution of octanethiol (1 mM) for 24 h or hexane solution of octanethiol (1 mM) for 6 min, and rinsed with ethanol just before being inserted into the vacuum chamber for the STM observations.

In Chapter 5, we will discuss IETS for partially deuterated and fully deuterated alkanethiol SAMs. Partially deuterated alkanethiols were synthesized from commercially available $CD_3(CH_2)_7Br$ and $CH_3(CH_2)_6CD_2Br$ (C/D/N isotopes Inc., Canada) following the established scheme in [122]. Gas chromatography–mass spectrometry showed that the purity of the final product was 94.4 % ($CD_3(CH_2)_7SH$) and 98.7% ($CH_3(CH_2)_6CD_2SH$), respectively. Fully deuterated alkanethiol was purchased from C/D/N isotopes Inc. Partially-deuterated and fully deuterated alkanethiol SAMs were fabricated in the same way as for the normal octanethiol SAM.

4. STM-IETS for an alkanethiol SAM

4.1. Topographic image of an alkanethiol SAM

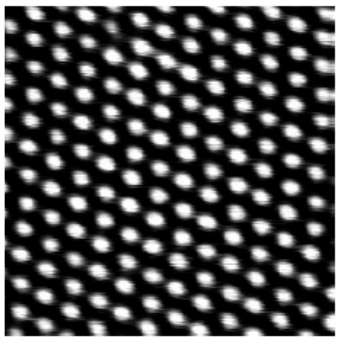

Fig. 12. Topographic STM image of an octanethiol SAM on the Au(111) (5.4 × 5.4 nm^2, I_t = 83 pA, and V_s = −2.5 V) [39].

Figure 12 shows a topographic image of the prepared octanethiol SAM on an Au(111) surface measured at 4.4 K, where the sample bias (V_s) and current (I_t) of the set point are V_s = −2.5 V and I_t = 83 pA, respectively [39]. As shown in the figure, we can see an ordered structure of the octanethiol SAM with ($\sqrt{3} \times \sqrt{3}$)R30° periodicity in relation to the substrate of Au(111), which is consistent with previous reports [3] and our theoretical simulations (see Fig. 6). Note that this well-ordered structure is usually observed before and after IETS measurements, i.e., the surface condition is confirmed in the case of STM-IETS.

4.2. Contact condition between the tip and molecule

The gap between the tip and molecule may be an important parameter for the IETS measurement. The I vs z curve shown in Fig. 13 was measured by approaching the tip at a rate of ~0.35 Å/s from the initial position (z = 0) defined by the conditions of I_t = 10 pA and V_s = 500 mV, where the vertical axis is expressed on a log scale [39]. We can fit the measured I vs z curve with a straight line at the initial stage of approach (z < −1.5 Å). This fitting curve can be expressed as $I \propto \exp(-\alpha z)$ with α = 2.0 Å^{-1}, where the decay constant, α, is comparable with those previously reported for the vacuum tunneling barrier of α = 2.4 Å^{-1} [123]. After reaching z = −1.5 Å, which gives I_t = ~0.2 nA at V_s = 500 mV, the curve shows a bend and is deviated from a straight line. The slope after the bend can be estimated as $I \propto \exp(-\beta z)$, with β = 1.1 Å^{-1} at its initial stage. However, β becomes smaller when the tip gets closer to the surface. The decay rate of the tunneling current through a monolayer of alkanethiol SAM was previously analyzed by Bumm et al. for SAMs with various chain lengths ($CH_3(CH_2)_{n-1}S$) [124]. They employed a two-layer model in which the vacuum layer and the SAM layer were assumed to have independent decay constants for the electron tunneling. They then reported that the tunneling current for the SAM layer was estimated to be $I \propto \exp(-\beta z)$ with β = 1.2 Å^{-1} [124]. We consider that the tip and the SAM contact at z = −1.5 Å and that the electron decay length in the SAM layer is close to the value that has been reported by Bumm et al. shortly after the contact. The decay length becomes smaller with any further approach of the tip, which we speculate to be due to a conformational change in the molecule layer caused by the tip.

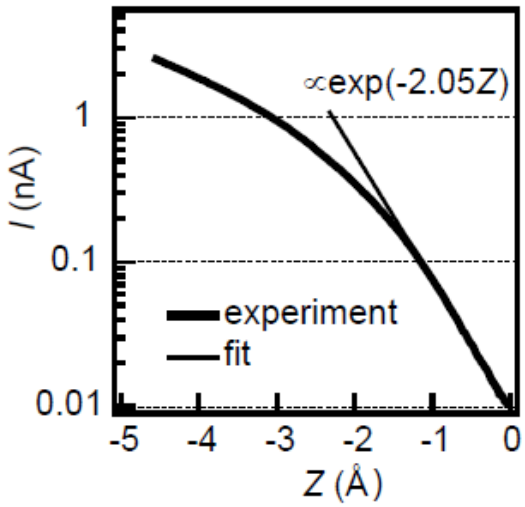

Fig. 13. Variation in the tunneling current when the tip approaches the surface (I vs z curve). The tip approached at a rate of ≈0.35 Å/s from the initial position of I_t = 0.01 nA and V_s = 500 mV. The linear line is the result of a least square fit with a function of $I \sim \exp(-\alpha z)$ [39].

4.3. IETS of an alkanethiol SAM using STM

In this section we show a typical IET spectrum for an octanethiol SAM on Au(111) at 4.4 K. Before commencing the IETS measurement we confirmed that a good topographic image could be obtained, such as that in Fig. 12, where the junction resistance is usually a few tens of GΩ. For the IETS measurement, the tip was placed on a bright spot of the STM image and was brought close to the surface to reduce the junction resistance to 0.5 GΩ (V_s = 500 mV, I_t = 1 nA). This set point is adopted because higher current is required for the IETS than the topographic imaging due to the limited signal. Judging from the I vs z curve in Fig. 13, at this set point the tip pushes the molecule layer about 1.5 Å from the contact point. Further lateral tracking of the tip position was not executed; however, the drift of the tip along the lateral direction was limited and was less than one unit of the alkanethiol lattice (5 Å) for 1 day. The data of I vs V, dI/dV vs V, and d^2I/dV^2 vs V were simultaneously recorded both for the increasing and decreasing voltage ramp between 500 and −500 mV, where the feedback loop was open for 14 min. For this interval, the current change due to the thermal drift along the vertical direction was usually less than 3%. The spectra in Fig. 14 are an average of 32 scans, each of which took 7 min, with the total acquisition time of about 4 h. A modulation voltage of 7.2 mV (rms) and a modulation frequency of 480 Hz were used. We confirmed that the tunneling current at 480 and 960 Hz contained no periodic noise by executing the fast Fourier transform of the tunneling current. The time constants of the two lock-in amplifiers were both set at 100 ms.

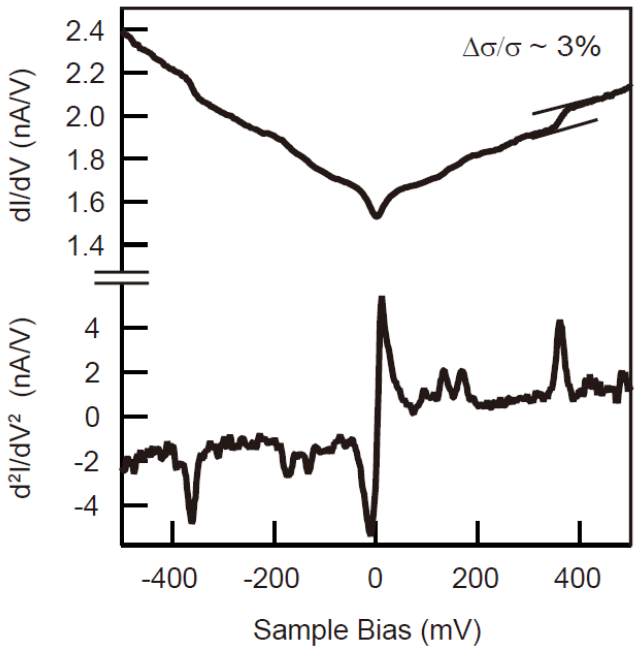

Fig. 14. Plot of d^2I/dV^2 vs. V for an octanethiol SAM on Au(111) at 4.4 K. The tip was positioned at I_t = 1 nA and V_s = 500 mV. A modulation voltage of V_{rms} = 7.2 mV has been added. The plot is an average of 32 cycles of measurements, taking ~7 min for each cycle [39].

The acquired d^2I/dV^2 vs V and dI/dV vs V plots are shown in Fig. 14 [39]. The vertical axis was calibrated by comparing the numerical differentiation of the I vs V and dI/dV vs V curves with the outputs of the lock-in amplifiers (see Section 4.4). As shown in Fig. 14, the d^2I/dV^2 vs V curve shows features that appear at symmetric energy positions about the Fermi level with a reversed polarity. These features satisfy conditions required to assign them as vibrational features [52]. Among several peaks originating from vibrational modes, we can see that a prominent feature appears at an energy of ±361 mV. Features at similar energies have been reported for STM-IETS studies of hydrocarbon molecules, such as C_2H_2 on Cu(100) [57,70] and *cis*- and *trans*-2-butene molecules on Pd(110) [58,59], which have been attributed to the C-H stretching mode (ν(C-H)). In all reports, the ν(C-H) feature dominates the IET spectra and other vibrational features are less obvious, except for the metal-molecule vibration modes [57–59,70]. On the other hand, the spectrum of Fig. 14 shows clear peaks between 50 and 200 meV. They also satisfy the criteria for assigning them to be vibration modes, and the vibrational modes in this energy range include C-H bending modes and a C-C stretching mode. The conductance change ($\Delta\sigma/\sigma$), estimated from dI/dV, is ~3.0% for the C-H stretching mode (361 mV) and ~1.2% for the CH bending mode (171mV). The measured $\Delta\sigma/\sigma$ for the C-H stretching mode exceeds 10% in the case of the C_2H_2 molecule [57]; however, other modes like C-H bending and C-C stretching were not detected. Thus, the detection of C-H bending and C-C stretching modes in the current study indicates a high yield of these modes in the case of the alkanethiol SAM. Precise assignment of these modes and reasons for the high yields are discussed in later sections.

4.4. Calibration of the IETS intensity

The black lines in Figs. 15(a), (b), and (c), show the I vs V, dI/dV vs V (output of the lock-in amplifier), and d^2I/dV^2 vs V (output of the lock-in amplifier), respectively [40]. The gray line in Fig. 15(b) is the numerical derivative of I vs V, from which the absolute value of dI/dV vs V with the lock-in amplifier is determined. The absolute value of d^2I/dV^2 with the lock-in amplifier (black line in Fig. 15(c)) is also determined by repeating the same process. Note that the fluctuation in the noise level of the dI/dV vs V and d^2I/dV^2 vs V curves by the lock-in amplifiers are smaller than those obtained by the numerical differentiation.

The dotted line in Fig. 15(b) is the output of the lock-in amplifier for the f component, where the phase is different by 90° from that of the black line in Fig. 15(b). The dotted line is almost constant for all of the bias voltages, indicating that the phase of the lock-in amplifier for the measurement of dI/dV vs V is correct. The capacitance between the tip and the sample, calculated from the magnitude of the dotted line, is 250 fF. The dotted line in Fig. 15(c) is the current component at $2f$ detected by the other lock-in amplifier where the phase is shifted by 90° from that of the black line in Fig. 15(c). It also shows that the magnitude of the dotted line is zero for all of the sample biases, which indicates that the phase for the d^2I/dV^2 vs V measurement is also correct.

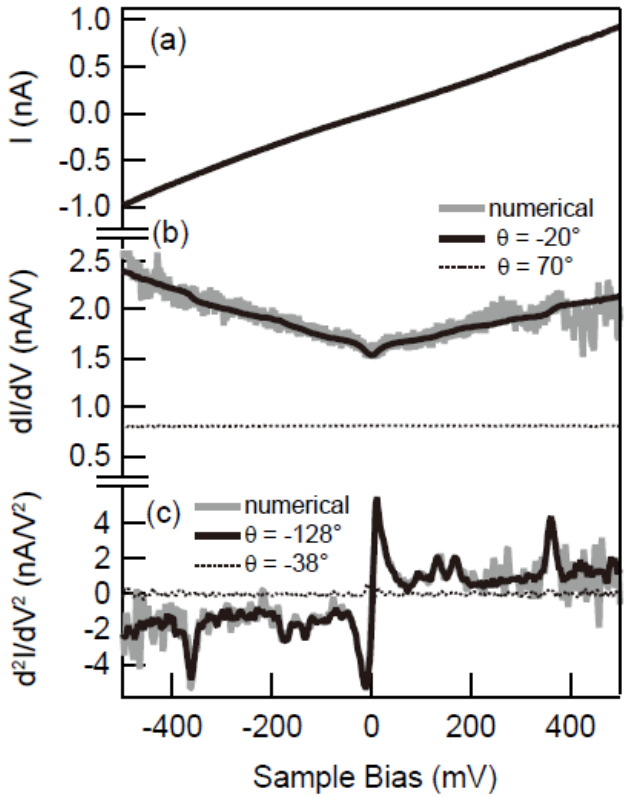

Fig. 15. (a) I vs V for the octanethiol SAM at 4.4 K (V_s = 500 mV, I_t = 1 nA). (b) The black line is dI/dV vs V acquired by the lock-in amplifier with the adjusted phase condition. The gray line is the numerical derivative of the I vs V. The dotted line is the output of the lock-in amplifier measuring the f component where the phase was 90° shifted from that in the case of the black line in Fig. 15(b). (c) The black line is d^2I/dV^2 vs V acquired by the other lock-in amplifier with the adjusted phase condition. The gray line is the numerical derivation of the dI/dV (black line in Fig. 15(b)). The dotted line is the output of the other lock-in amplifier measuring the 2f component where the phase is 90° shifted from that in the case of the black line in Fig. 15(c) [40].

4.5. Resolution of IETS

The full width at half maximum (FWHM) of the IET signal is described by the following formula:

$$W^2 = (1.7V_{\mathrm{mod}})^2 + (5.4kT/e)^2 + W_1^2, \tag{7}$$

where k is the Boltzmann constant, T is the temperature, V_{mod} is the modulation voltage (rms), and W_1 is the intrinsic width of the peak [125]. Figure 16(a) shows normalized d^2I/dV^2 vs V spectra in the energy range close to the C-H stretching mode of the octanethiol SAM (T = 4.4 K, V_s= 500 mV, I_t = 1 nA), where the modulation voltage was systematically varied from 25.2 to 5.2 mV (rms) [40]. The spectra were averaged over 24, 24, 24, 24, 32, and 112 scans for V_{mod} = 25.2, 21.6, 18.0, 14.4, 7.2, and 5.4 mV,

respectively. We can see that with a decrease in the modulation voltage, the peak width is also decreased. By further decreasing the modulation voltage to 2.7 mV, the peak seems to split into two components with peaks located at 359 mV and 365 mV (see Fig. 16(b)). In Fig. 16(b), both the positive and negative bias peaks are shown, where the sign of the IET signal for the negative bias is inverted. The spectra were averaged over 680 and 1,600 scans, which took about 11 and 27 h, for the positive sample bias and the negative sample bias, respectively. In Fig. 16(c), an IRA spectrum for the octanethiol SAM on the Au surface measured by our group is shown as a reference. This spectrum is similar to that shown in previous reports [20–22] with the following peak-assignment provided. Peak (*A*) at 354 meV is a CH_2 symmetric stretch, (*B*) at 357 meV is the CH_3 symmetric stretch by Fermi resonance, (*C*) at 362 meV is the CH_2 anti-symmetric stretch, (*D*) at 364 meV is the CH_3 symmetric stretch by Fermi resonance, and (*E*) at 368 meV is the CH_3 anti-symmetric stretch.

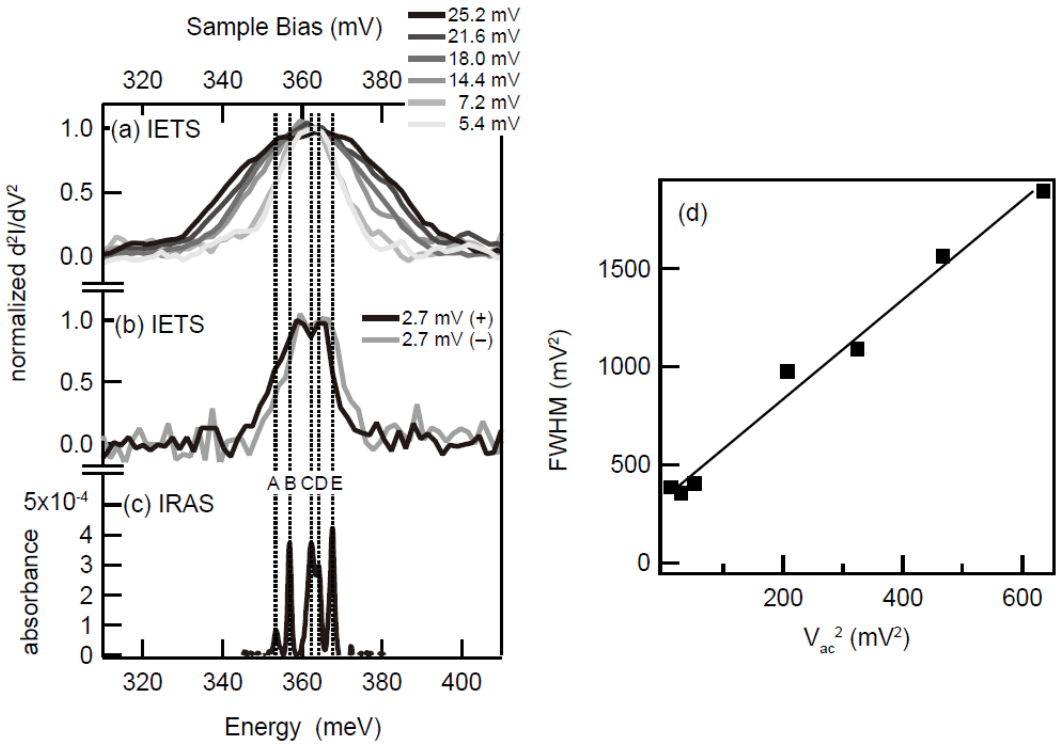

Fig. 16. (a) Normalized d^2I/dV^2 spectra around the energy of C-H stretching modes for the octanethiol SAM at 4.4 K, where the modulation voltage is systematically varied (V_s = 500 mV, I_t = 1 nA). (b) The same as Fig. 16(a), but in this case, the modulation voltage is 2.7 mV and the d^2I/dV^2 spectrum for negative bias is also shown. (c) Infrared reflection absorption spectrum for the octanethiol SAM on an Au surface at room temperature. (d) The square of FWHM of the CH stretching peak is plotted as a function of the square of the modulation voltage [40].

In the IET spectra with V_{mod} = 2.7 mV, we can see a saddle in Fig. 16(b). In order to further discuss the origin of these two peaks, it is required to employ a smaller modulation voltage and to obtain a spectrum of higher resolution. However, the

signal-to-noise ratio hampers the use of a smaller modulation bias voltage. Instead, we employed a partial deuteration method where all hydrogen atoms of the methyl group are replaced by deuterium atoms. This is discussed later in Section 5.4.

In Fig. 16(d), the squares of FWHM of the C-H stretching peaks are plotted as a function of the square of the modulation voltage [40]. The solid line is the result of a least square fitting of the experimental results expressed by $W^2 = (1.6V_{mod})^2 + 352$. This experimental observation is reproduced by Eq. (7), though due to experimental error there is a slight discrepancy in the prefactor of V_{mod}. This relationship between the FWHM and modulation voltage is consistent with the previous report for C_2H_2 molecules on Cu(100) [126]. Considering that $5.4kT/e$ = 2.0 mV at T = 4.4 K, W_1 is estimated to be 19 mV. This value is similar to the energy difference between Peak (*A*) and (*E*) in Fig. 16(c) (14 meV).

4.6. High-resolution IETS in the fingerprint region

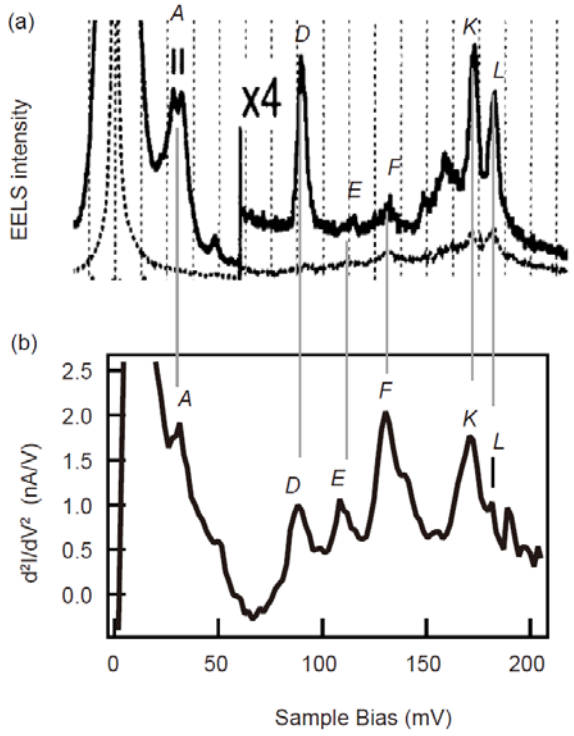

Fig. 17. (a) HR-EEL spectrum for an octanethiol SAM [23] and (b) high-resolution IET spectrum for the energy region of the C-C stretching mode and C-H bending mode of the octanethiol SAM (V_s = 500 mV, I_t = 1 nA, V_{mod} = 3.6 mV (rms), and T = 4.4 K) [39]. The peaks can be assigned as (*A*) Au-S stretching, (*D*) C-S stretching or CH_2 rocking, (*E*) CH_3 rocking, (*F*) C-C stretching, (*K*) CH_3 s-deformation or CH_2 wag, and (*L*) CH_2 scissor or CH_3 d-deformation.

In the previous section we showed that with a decrease in the amplitude of the modulation voltage, the IETS resolution of the C-H stretching mode is increased. The same thing can be seen for the vibrational modes in the fingerprint region, as shown in

Fig. 17 [39]. Here we employed a V_{mod} of 3.6 mV, which is half of that used in Fig. 15. The set point was V_s = 500 mV and I_t = 1 nA, and the temperature was 4.4 K. The data is an average of 464 scans, which took about 24 h to be collected. Reference EELS data is shown in Fig. 17(a), where we find that many vibrational peaks can be detected for both cases, indicating that IETS is a very effective characterization tool. The energy positions of the detected vibrational features are compared with the result of the HR-EELS, and the expected modes are listed in Table 1 with reference to HREELS, IRAS, and Raman spectroscopy [20–23,25]. By comparison to these spectroscopic data, we can assign the IETS peaks as follows: Peak (*A*) is Au-S stretching, (*D*) is C-S stretching or CH_2 rocking, (*E*) is CH_3 rocking, (*F*) is C-C stretching, (*K*) is CH_3 s-deformation or CH_2 wagging, and (*L*) is CH_2 scissoring or CH_3 d-deformation. For some peaks, such as peaks (*E*), (*K*), and (*L*), there are two candidates that can be discriminated using the technique of partial deuteration, as discussed later in Section 5.1.

Table. 1. The vibrational features of the current data are compared with EELS data [23] and the expected modes are listed with reference to the HREELS, IRAS, and Raman data [20–23,25].

peak	STM-IETS (meV)	EELS (meV)	Expected mode
A	31	28/32	Au-S stretch
D	88	81/89	ν(S-C) / CH_2 rock
E	108	113	CH_3 rock
F	130	130	ν(C-C)
K	171	172	CH_3 s-deform. / CH_2 wag
L	182	180	CH_3 d-deform. / CH_2 scissor

4.7. Comparison between experiment and theory

The overall property of the IET spectrum for an octanethiol SAM is compared to that obtained by theoretical calculation, as shown in Fig. 18 [41]. The IETS peaks deduced by both experiment and theory are approximately symmetric with the applied bias and the features of the IET spectrum can be divided into (i) the low bias anomaly caused by the large number of low-energy vibrations, including gold phonons, (ii) the fingerprint region (~50–200 meV) that includes ν(C-S), ν(C-C), and CH bending modes, which can be used to identify the molecule, and (iii) C-H stretch modes (ν(C-H) ~ 360 meV). Overall, the calculated IET spectrum reproduces that obtained by experiment. Exceptions are (i) the magnitude of the zero bias anomaly [81], where we note that the low-frequency vibrations originating from the Au(111) substrate are not included in the calculations, and (ii) the intensity of the ν(C-H) mode, which is severely underestimated by theory. To investigate the latter problem, we employed the partially deuterated alkanethiol and will discuss the origin of the difference in later sections (see Sections 5.4 and 5.5).

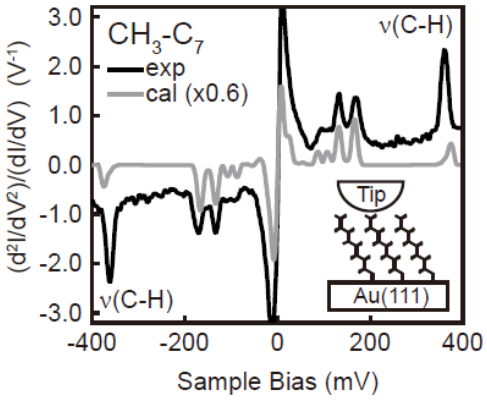

Fig. 18. Comparison between experimental (black) and calculated (gray) IET spectra for an octanethiol SAM. The broadening in both experiment and theory is determined by the temperature (4.4 K) and the lock-in modulation voltage (V_{mod} = 7.2 mV) [41].

4.8. Comparison to other tunneling junctions

Finally in this chapter, we compare the current results with the IETS data obtained using crossed-wire electrodes [81] and nanopore electrodes [28] (see Fig. 5). The IET spectra measured using crossed-wire electrodes show extraordinarily good agreement with our current data, both in terms of the energy-positions and the relative intensities of the peaks. The anomaly at low bias also shows good agreement. On the other hand, the comparison with the IET spectrum using nanopore electrodes shows few similarities: the relative intensity of the C-H stretching signal is low, with a derivative-like line shape of the peaks observed, and there are several unidentified peaks at around 250–500 meV. Recently, Yu et al. fabricated a molecular junction using a crossed-wire junction whereby metal impurities were intentionally incorporated among the molecules [111]. It was demonstrated that this junction with metal impurities shows similar peaks to those observed by Wang et al. [28], suggesting the possibility of the incorporation of metal impurities during the formation process of the top electrodes in the nanopore device. We should consider that the crossed-wire junction offers less damage for the alkanethiol molecules in the junctions.

5. IETS using isotope labeling

5.1. Precise assignment of IETS peaks by isotope labeling

As mentioned above, deuteration of a particular number of hydrogen atoms in an octanethiol SAM enables more precise assignment of the IETS peaks. Both partially deuterated alkanethiols and fully deuterated alkanethiols can form a SAM on Au(111) surfaces, where $(\sqrt{3} \times \sqrt{3})R30°$ periodicity in relation to the Au(111) substrate is observed, as is also the case for the normal alkanethiol.

The results of IETS for partially and fully deuterated octanethiols, including normal octanethiols, are summarized in Fig. 19 (V_s = 500 mV, I_t = 1 nA, and T = 4.4 K) [42]. We show the calculated energy positions of several anticipated vibrational modes for

those molecules in Fig. 19(b), where the vibrational modes (labeled *D*–*L*) are specified at the top. For the non-deuterated molecule, conclusive peak comparison with the experiment is hampered by the overlapping of peaks at similar energies. However, further analysis using the isotope-shift of the deuterated molecules enables a much more precise assignment to be made, wherein calculated isotope shifts (Fig. 19(b)) were compared to the corresponding IET spectra (Fig. 19(c)).

Among the expected vibrational peaks, some were not detected in the experimental IET spectra. We mark the detected peaks by solid lines and undetected peaks by dashed lines in Fig. 19(b). By this process, we can identify the dominant vibrational mode in the overlapping peaks. For example, (*E*) is composed of two overlapping peaks of the CH_3 rock and CH_2 twist modes in the non-deuterated molecule. These two modes are separated in energy by the deuteration of the methyl group [$CD_3(CH_2)_7$], but the CH_2 twist mode is not observed at the expected position. This result indicates a small yield for the CH_2 twist mode, and we conclude that peak (*E*) is dominated by the CH_3 rocking mode for the normal molecule. Through similar arguments we can assign peaks (*K*) and (*L*) to CH_2 wag and CH_2 scissor modes, respectively.

The fully deuterated molecule shows more complicated isotope shifts due to the coupling between the C-C stretching and CD bending modes. In this case we utilize the calculated IET spectra to identify peaks (*g*) and (*h*). Our calculation shows that peak (*g*) is a vibrational mode with the combined character of C-C stretching and CH_2 wagging, and peak (*h*) is a vibrational mode that accompanies the C-C stretch and CH_2 scissor. We can see that the character of the vibrational mode for fully deuterated alkanethiols is similar to that for the normal molecules.

We note that the calculated vibrational energies agree with those obtained by experiment within an accuracy of a few percent (see Table 2). In addition, both the relative peak heights and the absolute magnitude of the IETS peaks are well reproduced, the latter showing an agreement within a factor of three (although we have not considered additional broadening mechanisms).

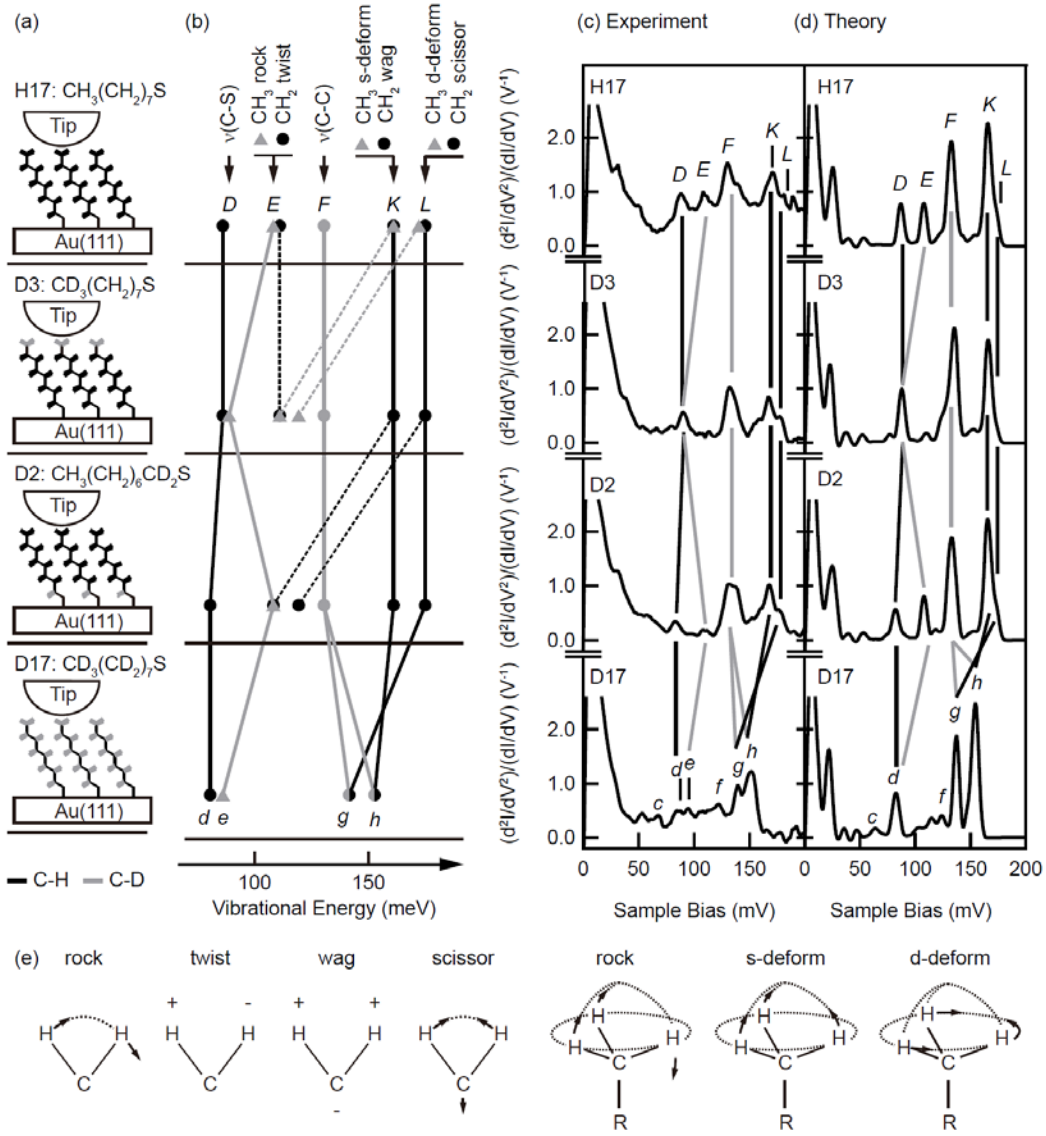

Fig. 19. IET spectra of deuterated alkanethiol SAMs. (a) Sketch showing the partial deuteration of C-H bonds, (b) calculated isotope shifts used to identify which vibrational modes contribute to the IET spectrum, (c) experimental IET spectra with the isotope shifts of individual IETS peaks highlighted, (d) calculated IET spectra using the NEGF-DFT method, (e) illustration of the various bending modes. In (b), the solid (dashed) lines correspond to observed (not observed) IETS modes (see text). The peaks *D*, *E*, *F*, *K*, and *L* originate from *ν*(S-C), CH_3 rocking, *ν*(C-C), CH_2 wagging, and CH_2 scissoring, respectively, and peaks *g* and *h* are *ν*(C-C) coupled with CD bending modes, see Table 2 for more details [42].

Table 2. Summary of IETS peaks.

Molecule	Mark	Exp. (meV)	Cal. (meV)	Main mode
$CH_3(CH_2)_7S$	*D*	88	87	ν(S-C)[*1]
	E	108	107	CH_3 rock
	F	130	132	ν(C-C)
	K	171	165	CH_2 wag[*2]
	L	182	173	CH_2 scissor[*3]
	M	361	368	ν(C-H)
$CD_3(CH_2)_7S$	*D/E*	90	88	ν(S-C)/CD_3[*4] rock
	F	132	135	ν(C-C)
	K	167	166	CH_2 wag
	L	178	172	CH_2 scissor
	i	255	256	$\nu_s(CD_3)$
		273	278	$\nu_{as}(CD_3)$
	M	360	364	ν(CH_2)
$CH_3(CH_2)_6CD_2S$	*D*	83[*5]	82[*5]	ν(S-C)[*1]
	E	108	108	CH_3 rock
	F	132	133	ν(C-C)
	K	169	165	CH_2 wag[*2]
	L	180	173	CH_2 scissor[*3]
	i	265	282	ν(C-D)
	M	360	374	ν(C-H)
$CD_3(CD_2)_7S$	*c*	68	63	CD_2 rock[*6]
	d	84[*5]	82[*5,*7]	ν(S-C)
	e	95	-	CD_3 rock[*8]
	f	123	124	CCC deform
	g	140	137	ν(C-C)[*9]
	h	152	154	ν(C-C)[*9]
	i	271	277	ν(C-D)

[*1,*2,*3]Overlap with small contributions from [*1]CH_2 rocking, [*2]CH_3 s-deformation, and [*3]CH_3 d-deformation. [*4]By deuteration of the methyl group, CH_3 rocking overlaps with peak *D*. [*5]Deuteration of the bottom methylene red-shifts the ν(S-C) mode by ~5 meV. [*6]Deuteration of the methylene groups shifts the CH_2 rocking mode, previously overlapping with peak *D*, to peak *c*. [*7]From theory, peak *d* originates from the prominent ν(C-S) at 82 mV and a weak CD_3 rocking mode at 85 mV. [*8]Assignment tentative. [*9]Coupled with CD bending modes. The isotope shifts in the full-deuteration case is not straightforward; sometimes the isotope shift couples modes, e.g., peaks *g* and *h* [42].

5.2. Propensity rule of IETS for an alkanethiol SAM

In the previous section we precisely assigned IETS active modes for alkanethiol molecules. Here, using Fermi's golden rule we discuss the reason why such modes are active in IETS. As mentioned in Section 2.4, the first eigenchannels with the largest transmission for the alkanethiol SAM have σ-type symmetry originating from the C-C bonds (see Fig. 7). These eigenchannels exponentially decrease as the electrons tunnel through the molecule. The σ-character, together with Eq. (4), implies a strong coupling of tunneling electrons to vibrational modes modifying the C-C bond lengths of the alkyl chain, since these modes also show σ-type symmetry. In fact, many of the IETS active modes, i.e., C-C stretch (peak *F*), CH_2 wag (*K*), and scissor (*L*), accompany a substantial displacement in the C-C bond length. In contrast, the inactive modes, CH_2 rock and twist, do not accompany a C-C displacement. By using this simple rule, we can also understand the strengths of the IETS signals, e.g., the scissor mode has less C-C character than the wagging mode, which is reflected in the IETS intensity.

5.3. Site selectivity of IETS for an alkanethiol SAM

Upon identification of the vibrational signals we can qualitatively understand how each part of a molecule contributes to the IET spectra. As shown in Fig. 19(c), the IETS intensity of peaks *F* (ν(C-C)), *K* (CH_2 wag), and *L* (CH_2 scissor) do not appreciably change with deuteration of the CH_2 closest to the sulfur atom ($CH_3(CH_2)_6CD_2S$). The IETS weight is therefore not predominantly determined from this part of the molecule, which is in contrast to the report by Beebe et al. [82].

A more quantitative discussion is possible by examining the C-H stretch modes. For the four alkanethiol molecules with different deuterated groups, the ν(C-D) and ν(C-H) regions of the IET spectra are shown in Fig. 20. In contrast to the fingerprint area, the comparison between experiment and theory for the C-H stretching region is not straightforward (see Section 4.7), we thus concentrate on the experimental results here. When we compare the non-deuterated and fully-deuterated case, see Fig. 20, it is seen that the C-H vibrational energy shows an isotope shift from 361 to 271 meV, closely matching the change in the effective mass. The IETS intensity in the fully-deuterated case also decrease by a factor of ~ $1/\sqrt{2}$. The decrease in IETS intensity might be due to the weakened e-ph coupling which is originated from the lowered vibration amplitude of the normal mode with the mass increase [45,74]. To estimate the size of the IET signals and quantify the position dependence, we integrate the experimental IET signals after subtracting the interpolated background indicated in Fig. 20(a). The resultant intensities are shown in Table 3. The integrated peak areas of the C-H stretching mode for the normal molecule and the C-D stretching modes for the fully-deuterated molecule are denoted by ν(C-H, all) and ν(C-D, all), respectively. In Table 3, we use these numbers to evaluate the relative weights of the ν(C-H) and ν(C-D) signals.

Table 3 shows, to a first approximation, that the C-H/C-D stretch signal originates with equal weights from all hydrogen atoms in the molecule, i.e., the signal is proportional to the number of H and D atoms. When the terminal methyl group is deuterated (Fig. 20(b)), the area of the ν(C-D, CD_3) peak is ~28% of ν(C-D, all), while the ν(C-H) peak is smaller than ν(C-H, all) by ~16%. Although there is a substantial discrepancy between the two numbers, the increase/decrease is roughly consistent with

a substitution ratio of 18% (3 out of 17 hydrogen atoms). We also find similar numbers for the methylene group, where the peak area of ν(C-D) is ~14% of ν(C-D, all) and the ν(C-H) reduction is ~23% of ν(C-H, all), which is comparable to 2/17 (~12%). Our finding that the signal is evenly generated throughout the molecule is also consistent with the above discussion for CH_2 wagging and CH_2 scissoring modes, where the contributions from the methylene group closest to the Au electrode are small. These discussions do not agree with the previous report [82] that the contribution of the methylene group closest to the electrode is notably enhanced due to its location close to the metal substrate. From a theoretical viewpoint, the exponential decay in the scattering states originating from the Au electrode and STM tip (see Fig. 7) will cancel in Fermi's golden rule, Eq. (4). Based on this picture, it is difficult to imagine that the IETS weights are significantly different for different parts of the molecule.

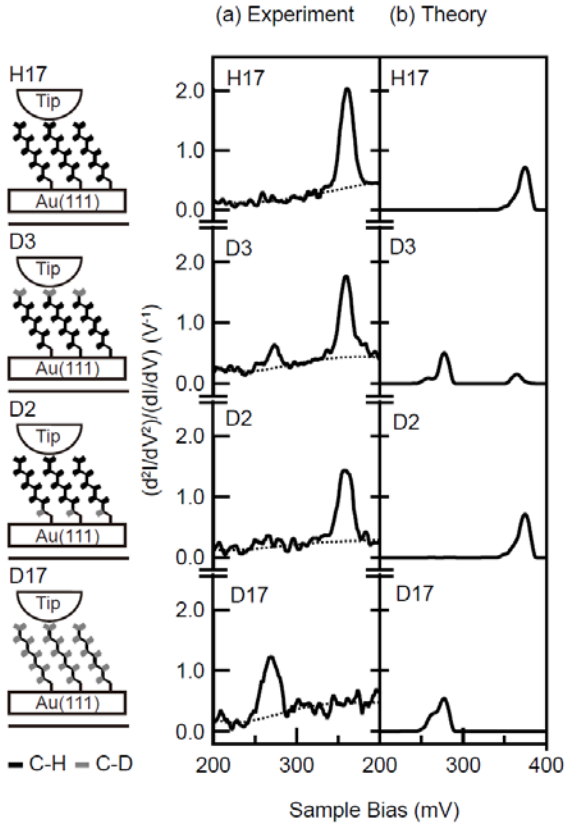

Fig. 20. ν(C-D) and ν(C-H) regions of IET spectra. Experimental (a) and theoretical (b) IET spectra for $CH_3(CH_2)_7S$ [H17], $CD_3(CH_2)_7S$ [D3], $CH_3(CH_2)_6CD_2S$ [D2], and $CD_3(CD_2)_7S$ [D17] (V_{rms} = 7.2 mV). The dotted lines in (a) show the estimated background signal [42]. For more details, see Tables 2 and 3.

Table 3. Relative peak area of ν(C-D) and ν(C-H) signals in the experiment. The standard (100%) of the ν(C-D) [ν(C-H)] signal is the peak area for $CD_3(CD_2)_7S$ [$CH_3(CH_2)_7S$] [42].

Molecule	ν(C-D)	ν(C-H)
$CH_3(CH_2)_7S$	-	100%
$CD_3(CH_2)_7S$	28%	84%
$CH_3(CH_2)_6CD_2S$	14%	77%
$CD_3(CD_2)_7S$	100%	-

5.4. C-H and C-D stretching signals

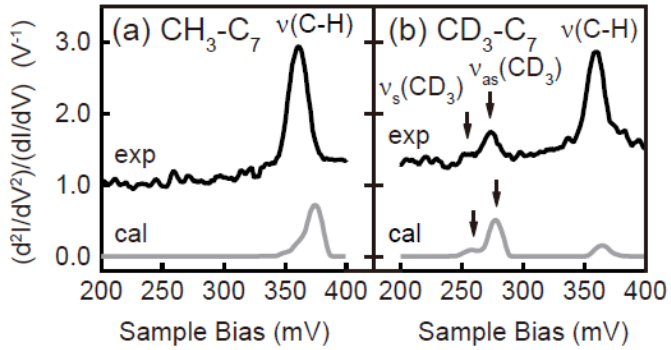

Fig. 21. IET spectra for the C-D and C-H stretch regions (ν(C-D) and ν(C-H)) for (a) CH_3-C_7 and (b) CD_3-C_7 SAMs on Au(111). The black and gray lines are the experimental and theoretical spectra, respectively (V_{mod} = 7.2 mV) [41].

As mentioned in Section 4.7, the intensity of the ν(C-H) mode deduced by the theory is severely underestimated compared to that found by experiment. Comparing the IET spectra of normal alkanethiol (hereafter denoted by CH_3-C_7) to the methyl group deuterated alkanethiol (hereafter denoted by CD_3-C_7) allows us to investigate this problem in more detail [41]. As shown in Fig. 21, the isotope shifted ν(C-D) signal was observed for CD_3-C_7 (Fig. 21(b)) but not for CH_3-C_7 (Fig. 21(a)), where we can see a small peak at 255 meV and a large peak at 273 meV. From comparison to IRAS data [127] and our calculations, we can assign the higher energy peak with the greater intensity to the asymmetric C-D stretching mode of CD_3 (275 meV by IR-$\nu_{as}(CD_3)$ [127] and 278 meV by theory) and the lower energy peak with lesser intensity to the symmetric C-D stretching mode of the CD_3 (258 meV by IR-$\nu_s(CD_3)$ [127] and 256 meV by theory). The measured peak area ratio of $\nu_{as}(CD_3)$ to $\nu_s(CD_3)$ were 80:20, which is estimated using Gaussian fitting. This value is comparable to the theoretical values of 84% and 16%, underlining the quantitative agreement for the CH_3 modes. Additional measurements on shorter alkanethiol (methyl-group deuterated hexanethiols: CD_3-$(CH_2)_5$-S) for different tip-sample distances shows that this dominance of the asymmetric mode in the ν(CD_3) IET signal is stable given that it is observed even when

a vacuum gap exists between the sample and the tip.

For macroscopic tunneling junctions (metal-insulator-molecule-metal), an empirical IETS selection rule has been suggested [52]. In these early IETS theories, tunneling electrons are assumed to interact with the dynamic dipole moments of a molecule via the long range Coulomb force [55]. The strength of these dipole moments will be enhanced by image charges when its direction points lie along the surface normal and reduced when its direction points lie parallel to the surface. Thus, one can argue that the main IET signal comes from the vibrational modes whose dynamic dipole moments point along the surface normal. Our measurements on the methyl group are inconsistent with this rule since the strong IET signal comes from the asymmetric CH_3 stretch mode which has a much smaller dynamic dipole moment along the surface normal than the symmetric stretch (see Section 1.2) [21].

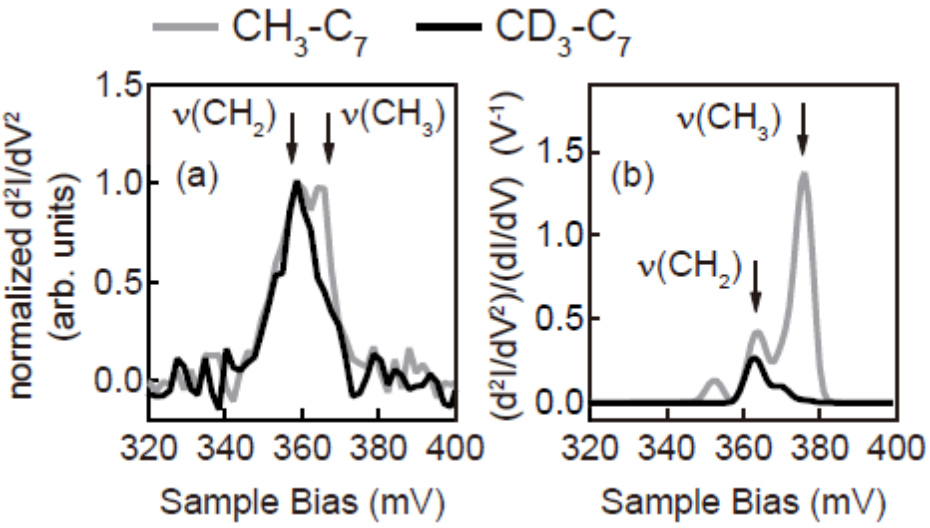

Fig. 22. (a) Experimental and (b) theoretical high-resolution IETS around the ν(C-H) modes for CH_3-C_7 (black) and CD_3-C_7 (gray) SAMs on Au(111) (V_{mod} = 2.7 mV). The experimental IETS intensity is normalized such that the peak height is 1 for both cases [39].

We also see changes in the ν(C-H) region of the IET spectra upon deuteration of the methyl group, which can aid the assignment of the modes in the ν(C-H) region. The black and gray lines in Fig. 22(a) show the high-resolution IET spectra for CH_3-C_7 and CD_3-C_7, respectively. To compare the experimental spectra we use a smaller lock-in voltage (V_{mod} = 2.7 mV, see Section 4.5) and normalize the peak heights. For the CH_3-C_7 (gray line), two peaks can be seen at energies of 359 meV and 365 meV, while for CD_3-C_7 (black line) we only observe a single peak whose energy is identical to that of the lower-energy component of the gray curve. The peak-area ratio of the low energy component to the high energy one was estimated using Gaussian functions to be 5:1. Since the ν(C-H) signal for the CD_3-C_7 molecule is expected to only originate from the CH_2 group, we can assign the components of 359 meV and 365 meV to the CH_2 and CH_3 groups, respectively. Taking into account the fact that using IRAS the CH_2 symmetric and asymmetric modes are observed at 354 and 362 meV, respectively

[21,22], our observation of a lower energy CH_2 IET peak centered at 359 meV indicates that the IET intensity is composed by the asymmetric and symmetric CH_2 stretch modes in an approximately equal contribution. Note that the symmetric C-H stretching mode of the CH_2 and the asymmetric C-H stretching mode of CH_2 are not distinguished in the IETS (see Fig. 22(a)) owing to the small energy splitting (8 meV), however, that is not the case for the C-D stretching mode of the CD_3 (see Fig. 21(b)) owing to the large energy splitting (17 meV). IRAS data further provides the symmetric and asymmetric stretch modes of the CH_3 group ($\nu_s(CH_3)$ and $\nu_{as}(CH_3)$) at 360 [128] and 367 meV. The latter value is close to the high-energy peaks of the IET spectra and is consistent with the conclusion that the asymmetric mode is dominant for the methyl group. The experimental data therefore indicate that (i) the majority of the C-H stretch IET signal originate from the CH_2 groups with (ii) approximately equal weights for $\nu_s(CH_2)$ and $\nu_{as}(CH_2)$, (iii) a smaller ratio (1:5) of the signal originates from the CH_3 group, for which (iv) the asymmetric CH_3 stretch dominates over the symmetric stretch mode.

5.5. Intermolecular and intramolecular tunneling

In the previous section we summarized the experimentally observed features of the C-H stretching signal. In the C-H stretching energy region (~350–380 meV), the comparison between results obtained by experiment and theoretical calculations is less satisfactory. For example, the calculated vibrational energies are consistently 5–10 meV larger than the experimental data ($\nu_s(CH_3)$ = 353 and 365 meV, $\nu_{as}(CH_3)$ = 375 meV, $\nu_s(CH_2)$ = 363 meV, and $\nu_{as}(CH_2)$ = 369 meV). In addition, the IETS amplitude for the $\nu(CH_2)$ mode is severely underestimated by theory (see Figs. 21 and 22) [41]. The quantitative agreement with experiments for the $\nu(CD_3)$ modes makes the poor performance for the $\nu(CH_2)$ modes particularly puzzling. However, one may propose the hypothesis that the discrepancy is due to inelastic intermolecular scattering, i.e., that the $\nu(CH_2)$ modes scatter the electrons tunneling between molecules of the SAM and/or that the $\nu(CH_2)$ vibrations of nearby molecules influence the transport through the molecule under the tip (see Fig. 23(a)). This idea can explain the poor agreement between theory and experiment since DFT is not well suited for describing intermolecular interactions. In addition, the magnitude of the e-ph coupling for the $\nu(CH_2)$ modes should be large between the molecules and could thus, according to Eq. (4), enable intermolecular hopping.

Our calculations, though they give a small IETS weight, indicate that intermolecular scattering is indeed important. As shown in Fig. 23(b), the majority of the current is carried by the elastic process whose energy-resolved current density [41], assuming a positive tip bias, is shown in Fig. 23(c). Here, approximately 75% of the current passes through the molecule closest to the tip (second molecule from the left in the figures), i.e., intramolecular tunneling (see Fig. 23(a)) is dominant in the elastic process. We have also studied the change in current densities due to inelastic scattering, with only the $\nu(CH_2)$ excitation process considered here. In this case, electrons start at E_{high} and end at E_{low} by exciting the vibration of $h\nu$ (see Fig. 23(b)). The current densities at E_{high} (before excitation) and E_{low} (after excitation) are shown in Figs. 23(d) and (e), respectively, where the former gradually decreases throughout the SAM as the electrons are scattered to E_{low}. In the inelastic tunneling case, 62% of the current enters through

the molecule closest to the tip (second molecule from the left in the figures). This value is lower than that found in the case of the elastic process and indicates that the electrons take a more intermolecular path than in the elastic process. In addition, Figs. 23(d) and (e) show a smaller part of the current entering the molecule under the tip (Fig. 23(d), second molecule from the left) than exiting (Fig. 23(e)), which also indicates that intermolecular scattering is important for exciting the $\nu(CH_2)$ mode.

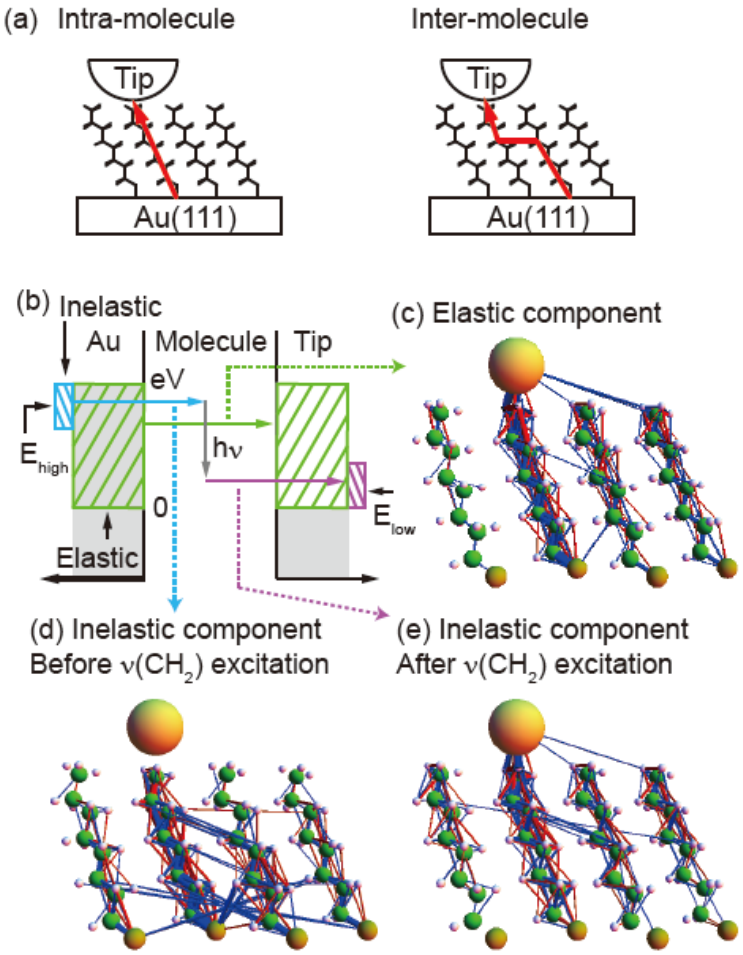

Fig. 23 (a) Intra- and intermolecular current paths, (b) schematics of the energy resolved elastic and inelastic processes. Current density plots of the elastic component (c) and inelastic components (d) before and (e) after the $\nu(CH_2)$ excitation, where the cylindrical area is proportional to the current density (normalized) and blue (red) indicates electrons flowing upwards (downwards) [41].

Here the intermolecular tunneling had been studied also for elastic process, where the conductivity of a SAM sample was measured with a conductive AFM [33,129,130]. It was reported that the conductivity of alkanethiol SAMs increased with increasing the tilt angle of molecules [33,129,130]. In order to understand this observation, Frederiksen et al., performed the first principles calculation for SAMs by changing the density of alkanethiol molecules on a substrate while keeping the SAM structure [130].

They found slight increase of conductance with increasing the molecular density, which supports the contribution of intermolecular tunneling.

Including the paper by Frederiksen et al. [130], our studies show that intermolecular scattering is taking place in the DFT calculations, however, it is not a definitive proof of the intermolecular scattering hypothesis and alternative explanations cannot be ruled out, e.g., supramolecular structures in the SAM, etc. The reason for the theoretical underestimation of the $\nu(CH_2)$ IETS intensity must therefore be studied further.

5.6. Contribution from molecules adsorbed on tip

In STM-IETS, the background signal of the measured spectra depends on the shape of a tip apex even when extraneous molecules do not adsorb on the tip apex. If a molecule adsorbs onto the tip apex, it can contribute to the IETS along with molecules on the metal substrate beneath the tip. These contributions originating from the tip shape and extraneous molecules on the tip make the interpretation of IETS complicated. However, such effects can be discriminated in usual STM-IETS by comparing the spectroscopy for a bare metal surface with that for a molecule on the metal surface [57]. For the SAM samples described in this article, however, it is difficult to adopt this method because the surfaces are fully covered with molecules composing SAMs, i.e., there is no bare metal region on the sample surface. Thus, we tried to eliminate these effects by changing the tip apex condition several times and averaging the data. We believe this process averages out the contributions that depend on the tip condition; however, IETS investigations combined with a tip characterization technique such as field ion microscopy [131] is required in order to further deepen our understanding on the IET processes for SAM surfaces.

6. Spatial distribution of IETS

6.1. Mapping of IET signal

Up to this point we have described the spectroscopic aspects of the inelastic process for alkanethiol SAMs. This IETS technique can be used to discriminate isotope molecules such as C_2H_2 and C_2D_2, and $^{12}C^{16}O$ and $^{13}C^{16}O$, with molecular resolution by measuring the spatial distribution of the IET signals [57,110]. Partial deuteration in the single molecule, such as the C-D bond in DC-CH, is also distinguished from the C-H bond in DC-CH by mapping of the IET signal [70]. Thus far, molecules with short bond lengths, like carbon monoxide and acetylene, have been employed to demonstrate the ability of IETS for chemical analysis with atomic resolution [57,110]. In most experimental situations, these short molecules are adsorbed on the metal surface with their axis parallel to the surface. Under this condition, scanning of an STM tip with a tunneling current of several nA is possible, providing large IET signals and good conditions for the mapping of IET signals. However, this is not the case when an alkanethiol SAM is employed as a sample, where each molecule stands upright to form a layer with large resistance. In this case, the newly proposed method of IET signal mapping (see Section 3.2) is effective.

6.2. Insertion of a hydrogenated alkanethiol into a matrix of deuterated alkanethiol

SAMs

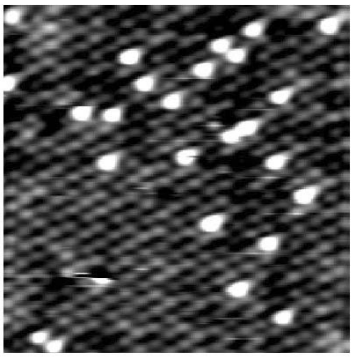

Fig. 24. STM image of a $CH_3(CH_2)_7S$ and $CD_3(CD_2)_5S$ coadsorbed SAM on Au(111). Sample bias of 1.5 V, current of 9 pA, scan area of 10 nm × 10 nm, temperature of 4.4 K. Bright and dim spots are identical to the hydrogenated octanethiols and deuterated hexanethiols, respectively. The ratio of the number of bright to dim spots is 1:19, which is almost identical to the ratio of the constituents (1:25) in the ethanol solution from which the SAM was prepared [43].

Mapping of IET signals for an alkanethiol SAM composed of hydrogenated alkanethiol (H-alkanethiol) and deuterated alkanethiol (D-alkanethiol) can provide information on the tunneling passage of electrons in the SAM. In order to execute this investigation, identification of the isotope molecule inserted into the matrix of alkanethiol is required. An SAM sample composed of H- and D- alkanethiol can be prepared by dipping the Au substrate into an ethanol solution containing a minority of H-alkanethiol and a majority of D-alkanethiol. If we change the length of the molecule, e.g., using $CH_3(CH_2)_7S$ as the H-alkanethiol and $CD_3(CD_2)_5S$ as the D-alkanethiol, we can confirm the mixture from a topographic image of the SAM surface (see Fig. 24). Here, bright and dim spots are identical to the H-octanethiols and D-hexanethiols, respectively. The ratio of the number of bright to dim spots is 1:19, which is almost identical to the ratio of the constituents (1:25) in the ethanol solution from which the SAM was prepared. This observation indicates that when the length of the molecule is similar, the minor molecule is inserted into the matrix of the major molecule in an isolated manner, i.e., phase separation does not occur, in contrast to the case of the SAM formed by two molecules with significantly different molecular lengths [132,133].

6.3. Mapping the IET signal for an alkanethiol SAM

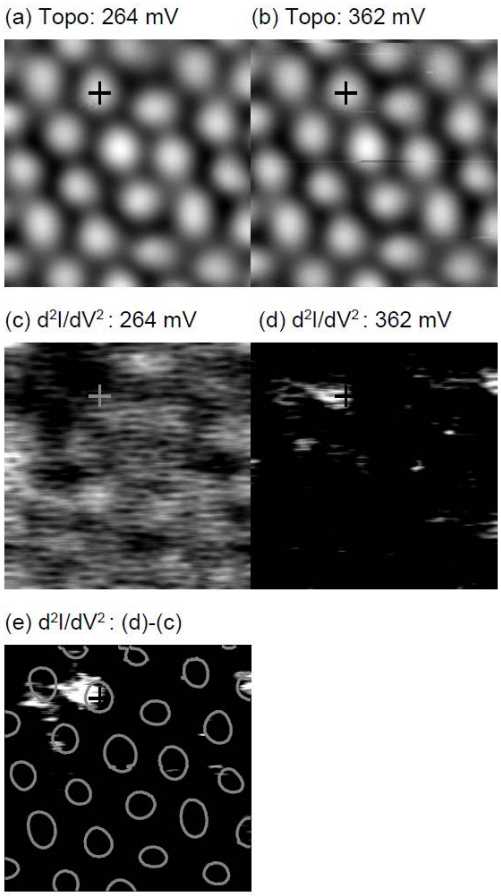

Fig. 25. STM images of $CH_3(CH_2)_5S$ and $CD_3(CD_2)_5S$ coadsorbed SAMs on Au(111) with a ratio of H:D = 1:9 for (a) V_s = 264 mV and I_t = 264 pA, and (b) V_s = 362 mV and I_t = 362 pA. The scan range is 2.2 nm × 2.2 nm. Maps of the IET signal with (c) V_s = 264 mV and (d) V_s = 362 mV, which were simultaneously measured with Figs. 25(a) and 25(b), respectively. (e) Difference between Fig. 25(d) and Fig. 25(c). Circles of gray lines represent the contour of the bright spot in the topographic image [43].

We next prepared samples where the lengths of the D-alkanethiol and H-alkanethiol were identical [43]. The ratio of the H-alkanethiol to D-alkanethiol in the solution was 1:9. Figs. 25(a) and (b) show topographic images of the thus prepared SAM surface with a sample bias of 264 mV (corresponding to the C-D stretching mode) and 362 mV (C-H stretching mode), respectively. No obvious differences in either topographic image can be seen, which is in contrast to the case of Fig. 24. Note that the lateral drift of the STM image was less than 0.2 Å in a single mapping process (1.4 h), therefore the scan areas of Fig. 25(a) and (b) are almost identical. Figs. 25(c) and (d) show the IET maps simultaneously acquired with topographic images of Figs. 25(a) and (b), respectively. In contrast to the identical topographic images, we can see a decrease in the signal from the C-D stretching mode at around the cross mark, see Fig. 25(c), and an

increase in the C-H stretching signal around the same mark, see Fig. 25(d).

This can be more clearly visualized by differentiating Figs. 25(c) and (d). By this method we can identify an H-hexanethiol molecule at the cross mark, see Fig. 25(e). There is an additional molecule in the upper right image that we attribute to an H-hexanethiol molecule, and thus we can identify two H-hexanethiol molecules out of a total of 25 molecules. This is a reasonable value considering that the mixture ratio of the H- to D-molecules was 1:9.

The tunneling resistance used in these IET maps was 1 GΩ (264 mV/264 pA or 362 mV/362 pA). When the resistance is lowered, the signal-to-noise ratio of the IET signals improves. However, this induces the problem of the interaction between the tip and sample. We used the tunneling resistance of several tens of GΩ for topographic imaging, which yielded good data in a routine manner. We speculate that a slight shift of the bright areas in the IET map and the topographic image is due to such tip-substrate interaction problems.

This problem may be solved by realizing a better signal-to-noise ratio in the tunneling current, which would allow us to use a smaller tunneling current and hence a wider tunneling gap. If this can be realized, the modulation voltage can be decreased from the current setting of 28.8 mV to a smaller value, which should contribute to visualizing the small energy differences between vibrational modes. This improved signal-to-noise ratio also clarifies the importance of the intermolecular tunneling process. The degree of the intermolecular process is shown by comparing the IET spectra for the case where the STM tip is above an H-alkanethiol molecule surrounded by D-alkanethiols with the case where the STM tip is placed above an H-alkanethiol molecule surrounded by the same H-alkanethiol molecules. Investigation of the intermolecular process using the IETS mapping technique is ongoing.

7. Summary

We have reviewed the recent progress made for the use of STM-IETS for alkanethiol SAMs. First, the theoretical framework and experimental methods were described in detail. IETS for alkanethiol SAMs was then demonstrated, where the many vibrational modes in the fingerprint region are detected as well as the large C-H stretching signal. This finding is similar to the results of HR-EELS, which indicates that IETS is an effective characterization method. Precise peak assignment was examined using the technique of isotope labeling, where we found that the IETS active modes accompany a substantial amount of C-C displacement. This finding is interpreted by Fermi's golden rule for IETS, taking into account the scattering states. Experimental results were quantitatively compared to those obtained by theoretical calculations, where the overall property of the IET spectrum and the fine features, such as the ratio of the symmetric CH_3 stretching signal to antisymmetric CH_3 stretching signal, are reproduced. The only exception to this is the large underestimation of the CH_2 stretching signal by calculation. In order to interpret this discrepancy, we proposed the hypothesis that the intermolecular tunneling process is important for producing the CH_2 stretching signal; however, this intermolecular process is underestimated by DFT. In the final section, we demonstrated the effectiveness of IET mapping for alkanethiol SAMs. Increasing the sensitivity of the IETS mapping methods is key to clarifying the importance of the intermolecular process.

Acknowledgements

The majority of the experiments described in this article were conducted at Tohoku University with Youhei Konda. We are deeply indebted to the collaboration. This study was partially supported by a Grant-in-Aid for Young Scientists (B) (23710113) from MEXT (N.O.).

References

[1] A. Ulman, Formation and structure of self-assembled monolayers, Chem. Rev., 96 (1996) 1533-1554.
[2] H.B. Akkerman, P.W.M. Blom, D.M. de Leeuw, B. de Boer, Towards molecular electronics with large-area molecular junctions, Nature, 441 (2006) 69-72.
[3] J.C. Love, L.A. Estroff, J.K. Kriebel, R.G. Nuzzo, G.M. Whitesides, Self-assembled monolayers of thiolates on metals as a form of nanotechnology, Chem. Rev., 105 (2005) 1103-1169.
[4] C. Vericat, M.E. Vela, G.A. Benitez, J.A.M. Gago, X. Torrelles, R.C. Salvarezza, Surface characterization of sulfur and alkanethiol self-assembled monolayers on Au(111), J. Phys.: Condens. Matter, 18 (2006) R867-R900.
[5] H.B. Akkerman, B. de Boer, Electrical conduction through single molecules and self-assembled monolayers, J. Phys.: Condens. Matter, 20 (2008) 013001-013020.
[6] A.S. Duwez, Exploiting electron spectroscopies to probe the structure and organization of self-assembled monolayers: a review, J. Electron Spectrosc. Relat. Phenom., 134 (2004) 97-138.
[7] A. Troisi, M.A. Ratner, Modeling the inelastic electron tunneling spectra of molecular wire junctions, Phys. Rev. B, 72 (2005) 033408-4.
[8] G.C. Solomon, A. Gagliardi, A. Pecchia, T. Frauenheim, A. Di Carlo, J.R. Reimers, N.S. Hush, Understanding the inelastic electron-tunneling spectra of alkanedithiols on gold, J. Chem. Phys., 124 (2006) 094704-094713.
[9] M. Paulsson, T. Frederiksen, M. Brandbyge, Inelastic transport through molecules: Comparing first-principles calculations to experiments, Nano Lett., 6 (2006) 258-262.
[10] R. Yamada, H. Wano, K. Uosaki, Effect of temperature on structure of the self-assembled monolayer of decanethiol on Au(111) surface, Langmuir, 16 (2000) 5523-5525.
[11] J. Noh, H.S. Kato, M. Kawai, M. Hara, Surface structure and interface dynamics of alkanethiol self-assembled monolayers on Au(111), J. Phys. Chem. B, 110 (2006) 2793-2797.
[12] J. Noh, M. Hara, Final phase of alkanethiol self-assembled monolayers on Au(111), Langmuir, 18 (2002) 1953-1956.
[13] G.E. Poirier, M.J. Tarlov, The C(4x2) Superlattice of N-Alkanethiol Monolayers Self-Assembled an Au(111), Langmuir, 10 (1994) 2853-2856.
[14] G.E. Poirier, M.J. Tarlov, H.E. Rushmeier, 2-Dimensional Liquid-Phase and the Px-Root-3-Phase of Alkanethiol Self-Assembled Monolayers on Au(111), Langmuir, 10 (1994) 3383-3386.
[15] A. Riposan, G.Y. Liu, Significance of local density of states in the scanning tunneling microscopy Imaging of alkanethiol self-assembled monolayers, J. Phys. Chem.

B, 110 (2006) 23926-23937.
[16] C.A. Alves, E.L. Smith, M.D. Porter, Atomic Scale Imaging of Alkanethiolate Monolayers at Gold Surfaces with Atomic Force Microscopy, J. Am. Chem. Soc., 114 (1992) 1222-1227.
[17] E. Barrena, E. Palacios-Lidon, C. Munuera, X. Torrelles, S. Ferrer, U. Jonas, M. Salmeron, C. Ocal, The role of intermolecular and molecule-substrate interactions in the stability of alkanethiol nonsaturated phases on Au(111), J. Am. Chem. Soc., 126 (2004) 385-395.
[18] P. Fenter, A. Eberhardt, K.S. Liang, P. Eisenberger, Epitaxy and chainlength dependent strain in self-assembled monolayers, J. Chem. Phys., 106 (1997) 1600-1608.
[19] D.G. Castner, K. Hinds, D.W. Grainger, X-ray photoelectron spectroscopy sulfur 2p study of organic thiol and disulfide binding interactions with gold surfaces, Langmuir, 12 (1996) 5083-5086.
[20] M.D. Porter, T.B. Bright, D.L. Allara, C.E.D. Chidsey, Spontaneously Organized Molecular Assemblies .4. Structural Characterization of Normal-Alkyl Thiol Monolayers on Gold by Optical Ellipsometry, Infrared-Spectroscopy, and Electrochemistry, J. Am. Chem. Soc., 109 (1987) 3559-3568.
[21] S.C. Chang, I. Chao, Y.T. Tao, Structures of Self-Assembled Monolayers of Aromatic-Derivatized Thiols on Evaporated Gold and Silver Surfaces - Implication on Packing Mechanism, J. Am. Chem. Soc., 116 (1994) 6792-6805.
[22] R.G. Nuzzo, L.H. Dubois, D.L. Allara, Fundamental-Studies of Microscopic Wetting on Organic-Surfaces .1. Formation and Structural Characterization of a Self-Consistent Series of Polyfunctional Organic Monolayers, J. Am. Chem. Soc., 112 (1990) 558-569.
[23] H.S. Kato, J. Noh, M. Hara, M. Kawai, An HREELS study of alkanethiol self-assembled monolayers on Au(111), J. Phys. Chem. B, 106 (2002) 9655-9658.
[24] R.G. Nuzzo, B.R. Zegarski, L.H. Dubois, Fundamental-Studies of the Chemisorption of Organosulfur Compounds on Au(111) - Implications for Molecular Self-Assembly on Gold Surfaces, J. Am. Chem. Soc., 109 (1987) 733-740.
[25] M.A. Bryant, J.E. Pemberton, Surface Raman-Scattering of Self-Assembled Monolayers Formed from 1-Alkanethiols - Behavior of Films at Au and Comparison to Films at Ag, J. Am. Chem. Soc., 113 (1991) 8284-8293.
[26] S. Masuda, Y. Koide, M. Aoki, Y. Morikawa, Local electronic properties induced at the molecule-metal interface, J. Phys. Chem. C, 111 (2007) 11747-11750.
[27] W.Y. Wang, T. Lee, M.A. Reed, Mechanism of electron conduction in self-assembled alkanethiol monolayer devices, Phys. Rev. B, 68 (2003) 035416-7.
[28] W.Y. Wang, T. Lee, I. Kretzschmar, M.A. Reed, Inelastic electron tunneling spectroscopy of an alkanedithiol self-assembled monolayer, Nano Lett., 4 (2004) 643-646.
[29] S. Gregory, Inelastic Tunneling Spectroscopy and Single-Electron Tunneling in an Adjustable Microscopic Tunnel Junction, Phys. Rev. Lett., 64 (1990) 689-692.
[30] J.G. Kushmerick, D.B. Holt, J.C. Yang, J. Naciri, M.H. Moore, R. Shashidhar, Metal-molecule contacts and charge transport across monomolecular layers: measurement and theory, Phys. Rev. Lett., 89 (2002) 086802-4.
[31] D.J. Wold, C.D. Frisbie, Formation of metal-molecule-metal tunnel junctions: Microcontacts to alkanethiol monolayers with a conducting AFM tip, J. Am. Chem. Soc., 122 (2000) 2970-2971.

[32] V.B. Engelkes, J.M. Beebe, C.D. Frisbie, Length-dependent transport in molecular junctions based on SAMs of alkanethiols and alkanedithiols: Effect of metal work function and applied bias on tunneling efficiency and contact resistance, J. Am. Chem. Soc., 126 (2004) 14287-14296.
[33] Y.B. Qi, I. Ratera, J.Y. Park, P.D. Ashby, S.Y. Quek, J.B. Neaton, M. Salmeron, Mechanical and charge transport properties of alkanethiol self-assembled monolayers on a Au(111) surface: The role of molecular tilt, Langmuir, 24 (2008) 2219-2223.
[34] M. Kiguchi, O. Tal, S. Wohlthat, F. Pauly, M. Krieger, D. Djukic, J.C. Cuevas, J.M. van Ruitenbeek, Highly conductive molecular junctions based on direct binding of benzene to platinum electrodes, Phys. Rev. Lett., 101 (2008) 046801-4.
[35] R.H.M. Smit, Y. Noat, C. Untiedt, N.D. Lang, M.C. van Hemert, J.M. van Ruitenbeek, Measurement of the conductance of a hydrogen molecule, Nature, 419 (2002) 906-909.
[36] M. Taniguchi, M. Tsutsui, K. Yokota, T. Kawai, Inelastic electron tunneling spectroscopy of single-molecule junctions using a mechanically controllable break junction, Nanotechnology, 20 (2009) 434008-8.
[37] A.S. Hallback, N. Oncel, J. Huskens, H.J.W. Zandvliet, B. Poelsema, Inelastic electron tunneling spectroscopy on decanethiol at elevated temoeratures, Nano Lett., 4 (2004) 2393-2395.
[38] R. Wiesendanger Scanning Probe Microscopy and Spectroscopy, Methods and Applications, Cambrigde University Press, Cambridge, 1994
[39] N. Okabayashi, Y. Konda, T. Komeda, Inelastic electron tunneling spectroscopy of an alkanethiol self-assembled monolayer using scanning tunneling microscopy, Phys. Rev. Lett., 100 (2008) 217801-4.
[40] N. Okabayashi, T. Komeda, Inelastic electron tunneling spectroscopy with a dilution refrigerator based scanning tunneling microscope, Meas. Sci. Technol., 20 (2009) 095602-8.
[41] N. Okabayashi, M. Paulsson, H. Ueba, Y. Konda, T. Komeda, Inelastic Tunneling Spectroscopy of Alkanethiol Molecules: High-Resolution Spectroscopy and Theoretical Simulations, Phys. Rev. Lett., 104 (2010) 077801-4.
[42] N. Okabayashi, M. Paulsson, H. Ueba, Y. Konda, T. Komeda, Site Selective Inelastic Electron Tunneling Spectroscopy Probed by Isotope Labeling, Nano Lett., 10 (2010) 2950-2955.
[43] N. Okabayashi, T. Komeda, Identification of a deuterated alkanethiol inserted in a hydrogenated alkanethiol self-assembled monolayer by mapping of an inelastic tunneling signal, Rev. Sci. Instrum., 81 (2010) 084101-4.
[44] M. Paulsson, T. Frederiksen, M. Brandbyge, Modeling inelastic phonon scattering in atomic- and molecular-wire junctions, Phys. Rev. B, 72 (2005) 201101-4.
[45] T. Frederiksen, M. Paulsson, M. Brandbyge, A.P. Jauho, Inelastic transport theory from first principles: Methodology and application to nanoscale devices, Phys. Rev. B, 75 (2007) 205413-205434.
[46] A. Kudelski, Characterization of thiolate-based mono- and bilayers by vibrational spectroscopy: A review, Vib. Spectrosc., 39 (2005) 200-213.
[47] W. Ho, Single-molecule chemistry, J. Chem. Phys., 117 (2002) 11033-11061.
[48] T. Komeda, Chemical identification and manipulation of molecules by vibrational excitation via inelastic tunneling process with scanning tunneling microscopy, Prog. Surf. Sci., 78 (2005) 41-85.

[49] M.A. Reed, Inelastic electron tunneling spectroscopy, Materials Today, 11 (2008) 46-50.
[50] M. Paulsson, T. Frederiksen, H. Ueba, N. Lorente, M. Brandbyge, Unified description of inelastic propensity rules for electron transport through nanoscale junctions, Phys. Rev. Lett., 100 (2008) 226604-4.
[51] R.C. Jaklevic, J. Lambe, Molecular Vibration Spectra by Electron Tunneling, Phys. Rev. Lett., 17 (1966) 1139-1140.
[52] P.K. Hansma, Tunneling Spectroscopy, Plenum Press, New York, 1982.
[53] D.G. Walmsley, J.L. Tomlin, Compilation of Inelastic Electron Tunnelling Spectra of Molecules Chemisorbed on Metal-Oxides, Prog. Surf. Sci., 18 (1985) 247-447.
[54] K.W. Hipps, U. Mazur, Inelastic Electron-Tunneling - an Alternative Molecular-Spectroscopy, J. Phys. Chem., 97 (1993) 7803-7814.
[55] D.J. Scalapino, S.M. Marcus, Theory of Inelastic Electron-Molecule Interactions in Tunnel Junctions, Phys. Rev. Lett., 18 (1967) 459-461.
[56] J. Lambe, R.C. Jaklevic, Molecular Vibration Spectra by Inelastic Electron Tunneling, Physical Review, 165 (1968) 821-832.
[57] B.C. Stipe, M.A. Rezaei, W. Ho, Single-molecule vibrational spectroscopy and microscopy, Science, 280 (1998) 1732-1735.
[58] Y. Sainoo, Y. Kim, T. Okawa, T. Komeda, H. Shigekawa, M. Kawai, Excitation of molecular vibrational modes with inelastic scanning tunneling microscopy processes: Examination through action spectra of cis-2-butene on Pd(110), Phys. Rev. Lett., 95 (2005) 246102-4.
[59] Y. Kim, T. Komeda, M. Kawai, Single-molecule reaction and characterization by vibrational excitation, Phys. Rev. Lett., 89 (2002) 126104-4.
[60] B.C. Stipe, M.A. Rezaei, W. Ho, Coupling of vibrational excitation to the rotational motion of a single adsorbed molecule, Phys. Rev. Lett., 81 (1998) 1263-1266.
[61] L.J. Lauhon, W. Ho, Single-molecule chemistry and vibrational spectroscopy: Pyridine and benzene on Cu(001), J. Phys. Chem. A, 104 (2000) 2463-2467.
[62] J.I. Pascual, J.J. Jackiw, Z. Song, P.S. Weiss, H. Conrad, H.P. Rust, Adsorbate-substrate vibrational modes of benzene on Ag(110) resolved with scanning tunneling spectroscopy, Phys. Rev. Lett., 86 (2001) 1050-1053.
[63] K.J. Franke, G. Schulze, J.I. Pascual, Excitation of Jahn-Teller Active Modes during Electron Transport through Single C(60) Molecules on Metal Surfaces, J Phys Chem Lett, 1 (2010) 500-504.
[64] K. Morgenstern, On the interpretation of IETS spectra of a small organic molecule, J. Phys.: Condens. Matter, 23 (2011) 484007-8.
[65] H. Gawronski, K. Morgenstern, K.H. Rieder, Electronic excitation of ice monomers on Au(111) by scanning tunneling microscopy - Vibrational spectra and induced processes, Eur. Phys. J. D, 35 (2005) 349-353.
[66] A. Strozecka, K. Muthukumar, J.A. Larsson, A. Dybek, T.J.S. Dennis, J. Myslivecek, B. Voigtlander, Electron-induced excitation of vibrations of Ce atoms inside a C(80) cage, Phys. Rev. B, 83 (2011) 165414-5.
[67] S. Katano, Y. Kim, M. Hori, M. Trenary, M. Kawai, Reversible control of hydrogenation of a single molecule, Science, 316 (2007) 1883-1886.
[68] T. Komeda, Y. Kim, M. Kawai, B.N.J. Persson, H. Ueba, Lateral hopping of molecules induced by excitation of internal vibration mode, Science, 295 (2002) 2055-2058.

[69] K. Motobayashi, Y. Kim, H. Ueba, M. Kawai, Insight into Action Spectroscopy for Single Molecule Motion and Reactions through Inelastic Electron Tunneling, Phys. Rev. Lett., 105 (2010) 076101-4.
[70] B.C. Stipe, H.A. Rezaei, W. Ho, Localization of inelastic tunneling and the determination of atomic-scale structure with chemical specificity, Phys. Rev. Lett., 82 (1999) 1724-1727.
[71] J.R. Hahn, W. Ho, Single molecule imaging and vibrational spectroscopy with a chemically modified tip of a scanning tunneling microscope, Phys. Rev. Lett., 87 (2001) 196102-4.
[72] L.J. Lauhon, W. Ho, Single-molecule vibrational spectroscopy and microscopy: CO on Cu(001) and Cu(110), Phys. Rev. B, 60 (1999) R8525-R8528.
[73] J.R. Hahn, H.J. Lee, W. Ho, Electronic resonance and symmetry in single-molecule inelastic electron tunneling, Phys. Rev. Lett., 85 (2000) 1914-1917.
[74] N. Lorente, M. Persson, Theory of single molecule vibrational spectroscopy and microscopy, Phys. Rev. Lett., 85 (2000) 2997-3000.
[75] N. Lorente, M. Persson, L.J. Lauhon, W. Ho, Symmetry selection rules for vibrationally inelastic tunneling, Phys. Rev. Lett., 86 (2001) 2593-2596
[76] T. Mii, S.G. Tikhodeev, H. Ueba, Spectral features of inelastic electron transport via a localized state, Phys. Rev. B, 68 (2003) 205406-5.
[77] N. Mingo, K. Makoshi, Calculation of the inelastic scanning tunneling image of acetylene on Cu(100), Phys. Rev. Lett., 84 (2000) 3694-3697.
[78] J.B. Maddox, U. Harbola, N. Liu, C. Silien, W. Ho, G.C. Bazan, S. Mukamel, Simulation of single molecule inelastic electron tunneling signals in paraphenylene-vinylene oligomers and distyrylbenzene[2.2]paracyclophanes, J. Phys. Chem. A, 110 (2006) 6329-6338.
[79] S. Monturet, M. Alducin, N. Lorente, Role of molecular electronic structure in inelastic electron tunneling spectroscopy: O(2) on Ag(110), Phys. Rev. B, 82 (2010) 085447-10.
[80] A. Garcia-Lekue, D. Sanchez-Portal, A. Arnau, T. Frederiksen, Simulation of inelastic electron tunneling spectroscopy of single molecules with functionalized tips, Phys. Rev. B, 83 (2011) 155417-10.
[81] J.G. Kushmerick, J. Lazorcik, C.H. Patterson, R. Shashidhar, D.S. Seferos, G.C. Bazan, Vibronic contributions to charge transport across molecular junctions, Nano Lett., 4 (2004) 639-642.
[82] J.M. Beebe, H.J. Moore, T.R. Lee, J.G. Kushmerick, Vibronic coupling in semifluorinated alkanethiol junctions: Implications for selection rules in inelastic electron tunneling spectroscopy, Nano Lett., 7 (2007) 1364-1368.
[83] J. Hihath, C.R. Arroyo, G. Rubio-Bollinger, N.J. Tao, N. Agrait, Study of electron-phonon interactions in a single molecule covalently connected to two electrodes, Nano Lett., 8 (2008) 1673-1678.
[84] J. Hihath, C. Bruot, H. Nakamura, Y. Asai, I. Diez-Perez, Y. Lee, L.P. Yu, N.J. Tao, Inelastic Transport and Low-Bias Rectification in a Single-Molecule Diode, ACS Nano, 5 (2011) 8331-8339.
[85] D.P. Long, A. Troisi, Inelastic electron tunneling spectroscopy of alkane monolayers with dissimilar attachment chemistry to gold, J. Am. Chem. Soc., 129 (2007) 15303-15310.
[86] D.P. Long, J.L. Lazorcik, B.A. Mantooth, M.H. Moore, M.A. Ratner, A. Troisi, Y.

Yao, J.W. Ciszek, J.M. Tour, R. Shashidhar, Effects of hydration on molecular junction transport, Nat. Mater., 5 (2006) 901-908.
[87] H. Song, Y. Kim, Y.H. Jang, H. Jeong, M.A. Reed, T. Lee, Observation of molecular orbital gating, Nature, 462 (2009) 1039-1043.
[88] C.R. Arroyo, T. Frederiksen, G. Rubio-Bollinger, M. Vélez, A. Arnau, D. Sánchez-Portal, N. Agraït, Characterization of single-molecule pentanedithiol junctions by inelastic electron tunneling spectroscopy and first-principles calculations, Phys. Rev. B, 81 (2010) 075405-5.
[89] R. Arielly, A. Ofarim, G. Noy, Y. Selzer, Accurate Determination of Plasmonic Fields in Molecular Junctions by Current Rectification at Optical Frequencies, Nano Lett., 11 (2011) 2968-2972.
[90] G. Noy, A. Ophir, Y. Selzer, Response of Molecular Junctions to Surface Plasmon Polaritons, Angew. Chem. Int. Ed., 49 (2010) 5734-5736.
[91] P. Yoon, M.M. Maitani, O.M. Cabarcos, L.T. Cai, T.S. Mayer, D.L. Allara, Crossed-Nanowire Molecular Junctions: A New Multispectroscopy Platform for Conduction-Structure Correlations, Nano Lett., 10 (2010) 2897-2902.
[92] M. Taniguchi, M. Tsutsui, K. Yokota, T. Kawai, Mechanically-controllable single molecule switch based on configuration specific electrical conductivity of metal-molecule-metal junctions, Chem Sci, 1 (2010) 247-253.
[93] M. Tsutsui, M. Taniguchi, K. Shoji, K. Yokota, T. Kawai, Identifying molecular signatures in metal-molecule-metal junctions, Nanoscale, 1 (2009) 164-170.
[94] S. Kaneko, T. Nakazumi, M. Kiguchi, Fabrication of a Well-Defined Single Benzene Molecule Junction Using Ag Electrodes, J Phys Chem Lett, 1 (2010) 3520-3523.
[95] T. Nakazumi, M. Kiguchi, Formation of Co Atomic Wire in Hydrogen Atmosphere, J Phys Chem Lett, 1 (2010) 923-926.
[96] Y. Asai, Theory of inelastic electric current through single molecules, Phys. Rev. Lett., 93 (2004) 246102-4.
[97] Y. Asai, Nonequilibrium phonon effects on transport properties through atomic and molecular bridge junctions, Phys. Rev. B, 78 (2008) 045434-24.
[98] T. Shimazaki, Y. Asai, Theoretical study of the lineshape of inelastic electron tunneling spectroscopy, Phys. Rev. B, 77 (2008) 115428-10.
[99] L.K. Dash, H. Ness, R.W. Godby, Nonequilibrium inelastic electronic transport: Polarization effects and vertex corrections to the self-consistent Born approximation, Phys. Rev. B, 84 (2011) 085433-9.
[100] A. Korventausta, J. Meyer, J. Nieminen, Carrier wave effect in nonresonant inelastic scanning tunneling spectroscopy of molecules with delocalized frontier orbitals, Phys. Rev. B, 81 (2010) 245426-13.
[101] H. Nakamura, K. Yamashita, Systematic study on quantum confinement and waveguide effects for elastic and inelastic currents in atomic gold wire: Importance of the phase factor for modeling electrodes, Nano Lett., 8 (2008) 6-12.
[102] H. Nakamura, K. Yamashita, A.R. Rocha, S. Sanvito, Efficient ab initio method for inelastic transport in nanoscale devices: Analysis of inelastic electron tunneling spectroscopy, Phys. Rev. B, 78 (2008) 235420-18.
[103] M. Galperin, M.A. Ratner, A. Nitzan, Molecular transport junctions: vibrational effects, J. Phys.: Condens. Matter, 19 (2007) 103201-103281.
[104] A. Gagliardi, G.C. Solomon, A. Pecchia, T. Frauenheim, A. Di Carlo, N.S. Hush,

J.R. Reimers, A priori method for propensity rules for inelastic electron tunneling spectroscopy of single-molecule conduction, Phys. Rev. B, 75 (2007) 174306-8.
[105] K. Shizu, T. Sato, K. Tanaka, Inelastic electron tunneling spectra and vibronic coupling density analysis of 2,5-dimercapto-1,3,4-thiadiazole and tetrathiafulvalene dithiol, Nanoscale, 2 (2010) 2186-2194.
[106] F. Demir, G. Kirczenow, Identification of the atomic scale structures of the gold-thiol interfaces of molecular nanowires by inelastic tunneling spectroscopy, J. Chem. Phys., 136 (2012) 014703-12.
[107] A. Troisi, M.A. Ratner, Molecular transport junctions: Propensity rules for inelastic electron tunneling spectra, Nano Lett., 6 (2006) 1784-1788
[108] M. Paulsson, C. Krag, T. Frederiksen, M. Brandbyge, Conductance of Alkanedithiol Single-Molecule Junctions: A Molecular Dynamics Study, Nano Lett., 9 (2009) 117-121.
[109] N. Agrait, C. Untiedt, G. Rubio-Bollinger, S. Vieira, Onset of energy dissipation in ballistic atomic wires, Phys. Rev. Lett., 88 (2002) 216803-4.
[110] A.J. Heinrich, J.A. Gupta, C.P. Lutz, D.M. Eigler, Single-atom spin-flip spectroscopy, Science, 306 (2004) 466-469.
[111] L.H. Yu, C.D. Zangmeister, J.G. Kushmerick, Origin of discrepancies in inelastic electron tunneling spectra of molecular junctions, Phys. Rev. Lett., 98 (2007) 206803-4.
[112] B.N.J. Persson, A. Baratoff, Inelastic Electron-Tunneling from a Metal Tip - the Contribution from Resonant Processes, Phys. Rev. Lett., 59 (1987) 339-342.
[113] J.H. Tian, B. Liu, X.L. Li, Z.L. Yang, B. Ren, S.T. Wu, N.J. Tao, Z.Q. Tian, Study of molecular junctions with a combined surface-enhanced Raman and mechanically controllable break junction method, J. Am. Chem. Soc., 128 (2006) 14748-14749.
[114] J. Steidtner, B. Pettinger, Tip-enhanced Raman spectroscopy and microscopy on single dye molecules with 15 nm resolution, Phys. Rev. Lett., 100 (2008) 236101-4.
[115] Z. Liu, S.Y. Ding, Z.B. Chen, X. Wang, J.H. Tian, J.R. Anema, X.S. Zhou, D.Y. Wu, B.W. Mao, X. Xu, B. Ren, Z.Q. Tian, Revealing the molecular structure of single-molecule junctions in different conductance states by fishing-mode tip-enhanced Raman spectroscopy, Nat Commun, 2 (2011) 305-6.
[116] J.M. Soler, E. Artacho, J.D. Gale, A. Garcia, J. Junquera, P. Ordejon, D. Sanchez-Portal, The SIESTA method for ab initio order-N materials simulation, J. Phys.: Condens. Matter, 14 (2002) 2745-2779.
[117] P. Ordejon, E. Artacho, J.M. Soler, Self-consistent order-N density-functional calculations for very large systems, Phys. Rev. B, 53 (1996) 10441-10444.
[118] M. Brandbyge, J.L. Mozos, P. Ordejon, J. Taylor, K. Stokbro, Density-functional method for nonequilibrium electron transport, Phys. Rev. B, 65 (2002) 165401-165417.
[119] M. Paulsson, M. Brandbyge, Transmission eigenchannels from nonequilibrium Green's functions, Phys. Rev. B, 76 (2007) 115117-7.
[120] Y.Y. Wang, E. Kioupakis, X.H. Lu, D. Wegner, R. Yamachika, J.E. Dahl, R.M.K. Carlson, S.G. Louie, M.F. Crommie, Spatially resolved electronic and vibronic properties of single diamondoid molecules, Nat. Mater., 7 (2008) 38-42.
[121] Y. Sainoo, Y. Kim, T. Komeda, M. Kawai, Inelastic tunneling spectroscopy using scanning tunneling microscopy on trans-2-butene molecule: Spectroscopy and mapping of vibrational feature, J. Chem. Phys., 120 (2004) 7249-7251.
[122] Z.F. Li, Z.R. Wu, F.Y. Luo, Synthesis and antifungal activities of alkyl

N-(1,2,3-thiadiazole-4-carbonyl) carbamates and S-alkyl N-(1,2,3-thiadiazole-4-carbonyl) carbamothioates, J. Agric. Food Chem., 53 (2005) 3872-3876.
[123] L. Olesen, M. Brandbyge, M.R. Sorensen, K.W. Jacobsen, E. Laegsgaard, I. Stensgaard, F. Besenbacher, Apparent barrier height in scanning tunneling microscopy revisited, Phys. Rev. Lett., 76 (1996) 1485-1488.
[124] L.A. Bumm, J.J. Arnold, T.D. Dunbar, D.L. Allara, P.S. Weiss, Electron transfer through organic molecules, J. Phys. Chem. B, 103 (1999) 8122-8127.
[125] J. Klein, A. Leger, M. Belin, Defourne.D, M.J. Sangster, Inelastic-Electron-Tunneling Spectroscopy of Metal-Insulator-Metal Junctions, Phys. Rev. B, 7 (1973) 2336-2348.
[126] L.J. Lauhon, W. Ho, Effects of temperature and other experimental variables on single molecule vibrational spectroscopy with the scanning tunneling microscope, Rev. Sci. Instrum., 72 (2001) 216-223.
[127] E. Garand, J.F. Picard, P. Rowntree, Inter- and intramolecular temperature-dependent vibrational perturbations of alkanethiol self-assembled monolayers, J. Phys. Chem. B, 108 (2004) 8182-8189.
[128] Average of the two Fermi resonance peaks at 357 and 364 meV.
[129] H. Song, H. Lee, T. Lee, Intermolecular chain-to-chain tunneling in metal-alkanethiol-metal junctions, J. Am. Chem. Soc., 129 (2007) 3806-3807.
[130] T. Frederiksen, C. Munuera, C. Ocal, M. Brandbyge, M. Paulsson, D. Sanchez-Portal, A. Arnau, Exploring the Tilt-Angle Dependence of Electron Tunneling across Molecular Junctions of Self-Assembled Alkanethiols, ACS Nano, 3 (2009) 2073-2080.
[131] G.L. Kellogg, Field-Ion Microscope Studies of Single-Atom Surface-Diffusion and Cluster Nucleation on Metal-Surfaces, Surf. Sci. Rep., 21 (1994) 1-88.
[132] S.F. Chen, L.Y. Li, C.L. Boozer, S.Y. Jiang, Controlled chemical and structural properties of mixed self-assembled monolayers of alkanethiols on Au(111), Langmuir, 16 (2000) 9287-9293.
[133] A.V. Shevade, J. Zhou, M.T. Zin, S.Y. Jiang, Phase behavior of mixed self-assembled monolayers of alkanethiols on Au(111): A configurational-bias Monte Carlo simulation study, Langmuir, 17 (2001) 7566-7572.